Mitigation of satellite OCO-2 CO_2 biases in the vicinity of clouds with 3D calculations using the Education and Research 3D Radiative Transfer Toolbox (EaR³T)

Yu-Wen Chen[a,b], K. Sebastian Schmidt[a,b], Hong Chen[b], Steven T. Massie[b], Susan S. Kulawik[c], and Hironobu Iwabuchi[d]

[a] *Department of Atmospheric and Oceanic Science, University of Colorado Boulder, Boulder, CO, US*
[b] *Laboratory for Atmospheric and Space Physics, University of Colorado, Boulder, CO, US*
[c] *Bay Area Environmental Research Institute, Earth Science Division, NASA Ames Research Center, Moffett Field, CA, US*
[d] *Center for Atmospheric and Oceanic Studies, Graduate School of Science, Tohoku University, Sendai, Miyagi, Japan*

Correspondence: Yu-Wen Chen (Yu-Wen.Chen@colorado.edu) and K. Sebastian Schmidt (Sebastian.Schmidt@lasp.colorado.edu)

Abstract. Accurate and continuous measurements of atmospheric carbon dioxide (CO_2) are essential for climate change research and monitoring of emission reduction efforts. NASA's Orbiting Carbon Observatory (OCO-2/3) satellites have been deployed to infer the column-averaged CO_2 dry air mixing ratio (X_{CO2}) from passive spectroscopy, with a designed uncertainty of less than one ppm for the regional average. This accuracy is often not met in cloudy regions because clouds in the vicinity of a footprint introduce biases in the X_{CO2} retrievals. These arise from limitations in the one-dimensional (1D) forward radiative transfer (RT) model, which does not capture the spectral radiance perturbations introduced by clouds adjacent to a clear footprint. Our paper introduces a three-dimensional (3D) RT pipeline to explicitly account for these effects in real-world satellite observations. This is done by ingesting collocated imagery and reanalysis products to calculate the cloud-induced perturbations at the footprint level. To make that computationally feasible, a simple approximation for their spectral dependence is used. The calculated perturbations are then used to reverse (undo) the cloud vicinity effects at the radiance level, at which point the standard 1D OCO-2 retrieval code can be applied without modifications. For two cases over land, we demonstrate that this approach indeed reduces the X_{CO2} anomalies near clouds. We also characterize the dependence of the X_{CO2} footprint-level bias on the distance from clouds and other key scene parameters, such as surface reflectance. Although this dependence may be specific to cloud type, aerosols, and other factors, we illustrate how it could be parameterized to bypass our physics-based 3D-RT pipeline for use in an operational framework. In the future, we intend to explore this possibility by applying our tool to a variety of scenes over land and ocean.

1. Introduction

Precise global carbon dioxide (CO_2) measurements are essential for a deeper understanding of surface CO_2 sources and sinks and their response to climate change, emissions reductions, and other mitigation strategies. The Greenhouse Gases Observing Satellites (GOSAT, GOSAT-2, Nakajima et al., 2010; Imasu et al., 2023) and the Orbiting Carbon Observatory (OCO-2, OCO-3, Chris, 2015; Eldering et al., 2019), launched by the Japan Aerospace Exploration Agency (JAXA) and NASA, respectively, are currently in space to observe CO_2 and other greenhouse gases. They have been designed to precisely measure CO_2 column dry air mixing ratios (X_{CO2}) through the analysis of reflected

solar radiances in the oxygen A-band at 765 nm (O_2-A), as well as the weak and strong CO_2 bands near 1.61 μm (WCO2) and 2.06 μm (SCO2).

High accuracy is imperative for remote sensing measurements of X_{CO2} to effectively contribute to carbon flux (sources and sinks) studies. Miller et al. (2007) suggest that the regional uncertainty should be within 0.3-0.5% (1 to 2 ppm) to meaningfully contribute to carbon flux estimates. Deng et al. (2016) and Crowell et al. (2018) highlight the importance of achieving high X_{CO2} measurement accuracy for reliable CO_2 flux estimation. Deng et al. (2016) show that the assimilation of GOSAT X_{CO2} data with a precision of approximately 0.5–1.0 ppm can significantly improve regional CO_2 flux estimates over land and ocean. Similarly, Crowell et al. (2018) emphasize that an X_{CO2} precision of 0.5–1.0 ppm is essential for detecting regional flux perturbations, especially in cloud-prone and high-latitude regions where CO_2 fluxes are difficult to constrain accurately using ground-based sensors alone. Precision and accuracy in CO_2 remote sensing are contingent on factors including spectroscopy, calibration, aerosol scattering and absorption, and atmospheric water vapor (Nelson et al., 2022; Worden et al., 2017; Connor et al., 2016). The OCO missions employ an X_{CO2} retrieval algorithm that integrates these elements along with observational conditions, such as solar zenith angle (SZA), viewing zenith angle, and geolocation (OCO-2 L2 ATBD, 2020), and uses a priori data such as CO_2 vertical profiles and surface reflectance to initialize spectral calculations via a computation-efficient one-dimensional (1D) radiative transfer (RT) model. The retrieval process iteratively refines the initial a priori estimates through optimal estimation methods (Rogers, 2000) until convergence between calculated and observed spectra is achieved.

Despite advancements in trace gas retrieval algorithms, the presence of clouds near satellite footprints remains a significant challenge. While retrievals typically exclude measurements over cloudy regions, photons scattered by nearby clouds can bias X_{CO2} retrievals due to the neglect of photon transfer between atmospheric columns in the 1D-RT model. Recent studies (Massie et al., 2017, 2021, 2023; Kylling et al., 2022) have highlighted the presence of the three-dimensional (3D) cloud bias in trace gas retrievals, including OCO and TROPOspheric Monitoring Instrument (TROPOMI) nitrogen dioxide (NO_2) retrievals. The cloud-related bias is also evident when examining individual footprints. With clouds covering roughly 70% of the globe (Wylie et al., 2005; King et al., 2013) and 40% of the OCO-2 measurements within 4 km of clouds (Massie et al., 2021), addressing cloud-induced bias is crucial for refining X_{CO2} retrieval accuracy.

Schmidt et al. (2019) explain that lateral photon transport represents missing physics in the operational OCO algorithm, and any adjustments for differences between 1D-RT and 3D-RT could introduce additional inaccuracies in X_{CO2} retrieval. Evaluating these differences requires a high-resolution 3D-RT model capable of simulating spectra across multiple wavelengths. Recent advancements have accelerated high-resolution 3D-RT simulations for multi-wavelength applications. For instance, Partain et al. (2000) introduced an enhanced implementation of the equivalence theorem, which decouples scattering and absorption calculations, allowing for accurate spectral integration without repeated multiple-scattering computations for Monte Carlo models. Emde et al. (2011) developed the Absorption Lines Importance Sampling (ALIS) technique, which efficiently computes high-resolution polarized spectra by leveraging Monte Carlo photon tracing across multiple wavelengths simultaneously. Iwabuchi and Okamura (2017) also adopted a similar way of using the same photon paths for various wavelengths to accelerate multi-wavelength 3D-RT simulation. Doicu et al. (2020) accelerated the Spherical Harmonics Discrete Ordinate Method (SHDOM) 3D-RT model, which is different from Monte-Carlo-based 3D radiative transfer models, by combining the correlated k-distribution method with dimensionality reduction techniques, such as principal component analysis.

While these acceleration methods have the potential to improve the accuracy of trace gas retrievals by taking into account missing physics (horizontal photon transport), current operational retrievals still do not use true 3D-RT in trace gas retrieval processes. Here, we adopt the approach introduced by Schmidt et al. (2019) as a practical method to approximate the 1D-RT and 3D-RT differences in spectral radiance observations, building on the concept of 3D-RT radiance perturbations, defined as the spectral percentage difference between 3D and 1D radiance simulations. These simulations in this study are performed by a modified version of the Education and Research 3D Radiative Transfer Toolbox (EaR³T; Chen et al., 2023), tailored specifically for OCO (EaR³T-OCO). The 3D perturbations proved to be a linear function of the radiance (or reflectance) itself across the relevant dynamic range of reflectance, which allows its representation by a simple slope and intercept for each of the three OCO-2 bands, with further details

---

164 provided in Section 2. We also introduce a "*bypass*" parameterization that relates slopes and intercepts to factors such
165 as cloud distance and scene reflectance, enabling the quantification of 3D cloud effects under varying conditions.
166   Although the reflectance-dependent physical mechanisms of the X_{CO2} 3D cloud retrieval bias are now largely
167 understood, strategies for applying these insights to bias correction have thus far been done empirically or statistically.
168 For example, Massie et al. (2022) proposed an empirical lookup table to correct 3D cloud biases based on a 3D metric,
169 and Mauceri et al. (2023) used machine learning techniques combined with TCCON observations. While both
170 approaches are operationally applicable, they rely on statistical corrections rather than the actual physical radiance
171 difference of the 3D cloud effect across the entire spectrum. In contrast, we present a new physics-based mitigation
172 framework that directly applies the linear representation of the 3D cloud effect to real OCO-2 observations. This
173 approach aims to remove the 3D perturbation at the radiance level before reapplying the operational 1D retrieval,
174 thereby improving the accuracy of the retrieved X_{CO2}.
175   The remainder of this paper is organized as follows: Section 2 provides background on the linear 3D
176 perturbation concept. Section 3 details data used in this study and EaR³T–OCO simulation. Section 4 (and Appendix B)
177 outlines our methodology for deriving slope and intercept parameters at a limited set of wavelengths and using them
178 to mitigate X_{CO2} biases. Section 5 shows how these parameters are used to correct the observed radiance spectra and,
179 by extension, the retrieved mitigated X_{CO2}. Finally, Section 6 provides conclusions, and Section 7 discusses future
180 work. Appendix C explains the functionality of EaR³T–OCO in detail.

2.   Background information

182 This study builds on Schmidt et al. (2019), which found a linear relationship between radiance perturbations and
183 reflectance due to 3D-RT effects. They define the 3D-RT radiance perturbation as the percent difference between the
184 radiances calculated by 3D and 1D radiative transfer models, as formulated in Eq. (1).
185

$$\text{Perturbation}_\lambda = \frac{I_\lambda^{3D} - I_\lambda^{IPA}}{I_\lambda^{IPA}} = \frac{I_\lambda^{3D}}{I_\lambda^{IPA}} - 1$$

186 (1)
187

188 The magnitude of this perturbation is not uniform across the observed wavelength spectrum, but depends on the
189 reflectance (R_λ), defined as follows:
190

$$R_\lambda = \frac{I_\lambda \times \pi}{S_0{}_\lambda^{TOA} \times \cos\theta_s}$$

191 (2)
192

193 where $S_0{}_\lambda^{TOA}$ in the denominator denotes the solar irradiance at the top of the atmosphere (TOA) for a given
194 wavelength λ, and θ_s is the solar zenith angle.
195   Within the dynamic range of interest for reflectance, the dependence of the perturbation on the reflectance is
196 linear. This is illustrated in Fig. 1, which shows simulated observations in the O₂-A band (Schmidt et al., 2019). For
197 small reflectance, the scatter increases, due to a limited number of photons in the calculations (Section 4.2.4). A line
198 is fitted to the data to represent the first-order dependence of the 3D-RT perturbation on the reflectance. This can be
199 done with either all wavelengths (grey dots) or a subset (red), which is strategically chosen to encompass the full
200 reflectance range.
201

$$\text{Perturbation}_\lambda = \frac{I_\lambda^{3D} - I_\lambda^{IPA}}{I_\lambda^{IPA}} \times 100\% =$$

289

290 Figure 1: Example of the linear relationship between perturbation and reflectance. The grey dots represent the
291 complete wavelength range, while the red dots indicate the subset selected for the O_2-A band simulation. The black
292 and red lines represent the linear fit of the grey and red dots, respectively.
293

294 The slope and intercept parameters, s_{xy} and i_{xy}, are obtained through weighted linear regression as shown in Eq. (3),
295 where the weights are the inverse of the perturbation uncertainty (computational noise, see Section 4.2.4). The slope
296 and intercept indicate distinct physical phenomena: a non-zero slope corresponds to wavelength-dependent variations
297 and differences in 1D and 3D radiances, photon path lengths, and absorption. Multiple scattering in 3D-RT increases
298 the photon path lengths and enhances absorption across different wavelengths, leading to non-zero perturbations, as
299 expressed by Eq. (1) (percentage differences between 1D and 3D radiances). This effect is more pronounced at
300 wavelengths with higher absorption, which experience greater attenuation compared to those with weaker absorption
301 for the same photon path length. As a result, the perturbations vary depending on the reflectance and absorption depth,
302 a phenomenon referred to as *spectral distortion* in our study. The intercept is related to the often-reported increase of
303 reflectance near clouds or decrease in shadows, whereas the slope accounts for spectroscopic effects for a small
304 spectral range, where the scattering effect can be considered spectral-independent.
305

306 $$Perturbation_\lambda = i_{xy} + s_{xy} \times R_\lambda^{3D} \quad (3)$$

307 ## 3. DATA

308 ### 3.1. OCO-2 data

309 Version 10r OCO-2 data, hosted by NASA's Goddard Earth Science Data and Information Services Center (GES
310 DISC) data archive (https://oco2.gesdisc.eosdis.nasa.gov/data/OCO2_DATA), are used in this research. The Level 1B
311 calibrated and geolocated science radiance spectra (L1bScND) are specified in all three OCO-2 bands, facilitating
312 simulation comparison and retrieval adjustment. Additionally, solar zenith and azimuth angles, as well as viewing
313 zenith and azimuth angles from this product, serve as inputs for the simulation. The standard Level 2 geolocated X_{CO2}
314 retrieval results (L2StdND) provide the retrieved CO_2 dry air mixing ratio and surface reflectance information for the
315 three bands. Note that the X_{CO2} in L2StdND files is raw X_{CO2} before the bias correction provided by the algorithm
316 team. We also employed Level 2 meteorological parameters interpolated from the global assimilation model for each

333   sounding (L2MetND) and Level 2 CO_2 prior based on the CO_2 monthly flask record, global meteorology, and age of
334   air (L2CO2Prior) to construct the atmosphere for the simulation (refer to Section 4.1.1.1).

335   ## 3.2.   MODIS Aqua data

336   The MODIS Aqua satellite, launched in May 2002, is part of NASA's A-Train constellation but exits the formation
337   due to fuel issues. As MODIS Aqua shared the same orbit as OCO-2 and arrived at the same scene approximately six
338   minutes after OCO-2, the collocated information from MODIS Aqua offers valuable insights into the meteorological
339   and surface conditions of the OCO-2 footprints and the spatial distances of clouds to the footprints. Several products
340   derived from MODIS Aqua observations are used in this study, including MODIS level 1B radiance products at the
341   quarter, half, and one-kilometer scales (channels 1 to 7, MYD02QKM, MYD02HKM, and MYD021KM, MODIS
342   Characterization Support Team (MCST), 2017a-c), the geolocation product (MYD03, MODIS Characterization
343   Support Team (MCST), 2017d), the level 2 cloud product (MYD06, Platnick et al., 2015), the level 2 aerosol product
344   (MYD04_L2, Levy et al., 2015) and the surface reflectance product (MCD43A3, Schaaf et al., 2021) from data
345   collection 6.1. These various products contribute to a comprehensive understanding of the atmospheric and surface
346   conditions relevant to the OCO-2 measurements, thereby enhancing the accuracy and reliability of our analysis.

347   # 4.   Methods

348   ## 4.1.   Case Description

349   In order to investigate the X_{CO2} retrieval biases resulting from cloud scattering, we have selected a case that features
350   high X_{CO2} anomalies in close proximity to clouds, as shown in Fig. 2. The chosen case is located in Central Asia,
351   spanning from 33.85° N, 55.15° E to 34.30° N, 55.45° E. The study focuses on the conditions observed on October
352   18th, 2018, with stronger reflectance for all three OCO-2 bands. The surface level based on the MODIS MYD03 file
353   is shown in Fig. A1, with the OCO-2 Met file specifying an average altitude near 790 m. The average solar zenith
354   angle and observation zenith angle for OCO-2 footprints are 48.5˚ and 0.31˚, and the mean surface albedo for O_2-A,
355   WCO_2, and SCO_2 bands are 0.288, 0.375, and 0.370, respectively. The average aerosol optical depth (AOD) at 550
356   nm from the MODIS MYD04 file is 0.179 over the domain. The appendix specifies the surface altitude level from the
357   MODIS MYD03 data file, plus the atmosphere profile for this case, derived by the method described in Section 4.2.1.1.
358
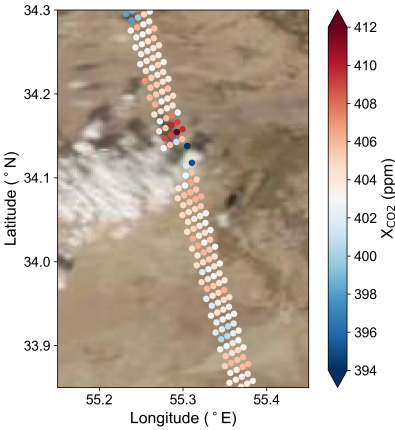
359

368 Figure 2: Satellite true-color imagery of MODIS Aqua from NASA Worldview on 18 October 2018, with OCO-2
369 retrieved X_{CO2} overlaid.

370 **4.2.   Overview of Radiative transfer model simulation**

371 The Education and Research 3D Radiative Transfer Toolbox v0.1.1 (Chen et al., 2023) for OCO (EaR³T-OCO) was
372 adapted to simulate 1D and 3D radiances for OCO-2 observations. The RT model simulates the photon-environment
373 interactions based on the understood physical mechanisms, such as absorption, scattering, and reflection. Since this
374 research aims to investigate the differences between 1D and 3D radiances, referred to as 3D radiative perturbations,
375 both 1D and 3D RT calculations are utilized. These perturbations, expressed as linear functions of reflectance, are
376 parameterized with slope and intercept values for each spectral band. The atmospheric environment used for the RT
377 simulation also impacts the results. Detailed descriptions of the atmospheric structure, vertical layering, and the
378 computation of number densities for absorption coefficients are provided in Appendix B.

379 **4.3.   Perturbations, Reflectance, Slopes, and Intercept Derivation**

380 Building on the foundational concepts of perturbation and reflectance introduced in Section 2 (refer to Eqs. 1-2), we
381 run the EaR³T-OCO simulator in 1D and 3D mode to calculate I_λ^{IPA} and I_λ^{3D}. From these simulated radiances, we
382 obtain the reflectances and perturbations. These are used to derive the slope and intercept parameters for quantifying
383 the 3D effect. We apply a weighted linear regression (see Eq. 3) to ensure that more accurate data exerts a greater
384 influence on the parameter estimation. This approach yields not only the slope and intercept values but also their
385 respective uncertainties, providing a comprehensive picture of the 3D effect's variability and reliability. The obtained
386 slope/intercept parameters are used to quantify the magnitude of the 3D effect, a detailed discussion of which is
387 presented in Sections 5.2 to 5.5. Additionally, the parameters play a crucial role in the offline mitigation strategies
388 explored in Section 5.6.

389 **4.4.   OCO retrieval algorithm and spectra mitigation**

390 The retrieval algorithm plays a vital role in determining X_{CO2} based on the radiances of the three bands. Notably, the
391 retrieval algorithm accounts for various processes, and post-retrieval processing calculates linear bias corrections
392 (O'Dell et al., 2018). Different retrieval versions may yield diverse outcomes even with identical inputs. In this study,
393 we utilize the corresponding OCO retrieval algorithm version B10.04 to compare with version 10r X_{CO2}. The retrieval
394 code is publicly available on NASA's GitHub repository (https://github.com/nasa/RtRetrievalFramework).

395 Given that the 1D-RT model does not account for additional scattered photons, the mitigation strategy
396 proposed in this study involves modifying the observed spectra to eliminate radiance changes induced by the 3D effect.
397 This adjustment process is referred to as "radiance adjustment" and is derived from Eqs. (1-3). Upon deriving the 3D
398 parameters in Section 4.3, we calculate the adjusted OCO-2 spectra ($I_\lambda^{IPA\,(adjusted)}$) using Eq. (4) with the observed
399 radiance spectra ($I_\lambda^{3D\,(obs)}$) and corresponding reflectance (R_λ^{obs}), slope (s_{xy}), and intercept (i_{xy}). Assuming the
400 absence of 3D effects in the adjusted 1D radiance, we can employ the B10.04 retrieval algorithm to the adjusted
401 spectra ($I_\lambda^{IPA\,(adjusted)}$) to obtain mitigated X_{CO2}.

402

$$I_\lambda^{IPA\,(adjusted)}(x,y) = \frac{I_\lambda^{3D\,(obs)}(x,y)}{(i_{xy} + s_{xy} \times R_\lambda^{obs} + 1)} \quad (4)$$

403
404

405 **5.   RESULTS**

5.1. 3D-RT simulation radiance closure

In order to derive the slope (**s**) and intercept (**i**) parameters that accurately represent the 3D cloud effect in the OCO-2 observations, it is crucial to perform realistic radiance simulations near the satellite's footprint. Chen et al. (2023) show that the extent of radiance closure (the percent difference in the forward radiance model and observed radiances) can indicate the correctness of the retrieved cloud properties. Fig. 3a-b presents the 3D-RT simulation and MODIS observation of 650 nm using the cloud optical thickness (COT), cloud effective radius (CER), and cloud top height (CTH) shown in Fig. A2. The heat map in Fig. 3c shows a good agreement between the simulation and observation, with an R^2 of 0.69 and a slope of 0.71. We then used the same CTH, CER, and COT settings to model the wavelengths in the O_2-A, WCO_2, and SCO_2 bands.
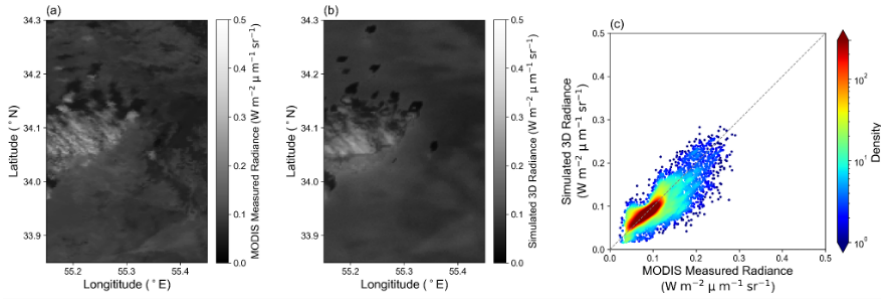
Figure 3: MODIS observation at 650 nm (a) and 3D radiance simulation at 650 nm by EaR³T (b). A heatmap comparison between (a) and (b) is depicted in (c).

Multiple reflectances or wavelengths are needed to derive **s** and **i** for the linear expression of the perturbations and reflectances of three bands. To balance computational demands with accuracy, we selected 11 wavelengths evenly distributed over the high 60% transmittance based on sorted clear-sky transmittance for further RT simulation (depicted in Fig. 4 as an example, the transmittance of full spectra is presented in Fig. A3). The transmittance is calculated based on the atmosphere profiles of pressure, temperature, gas optical depth, and aerosol/cloud optical properties. This reduction in simulated wavelengths is feasible due to the linear relationship between perturbations and reflectance. Employing a reduced number of wavelengths uniformly distributed across the reflectance space effectively minimizes computational demands while still permitting the derivation of **s** and **i** for the linear relationships within each band. Note that the number of wavelengths (11) utilized for determining the 3D parameters is adaptable. Employing additional wavelengths could decrease the uncertainty of the derived **s** and **i**, albeit at the expense of increased computation time.

Since the radiance simulation is cyclic at the edges, leaking radiance from one edge to the other could introduce unrealistic artifacts from RT simulations. We extended the margin by 0.15° on each side but excluded the additional margins during the analysis. Fig. A4 illustrates the simulation and the analysis domains with cloud distribution and cloud distance serving as the background.
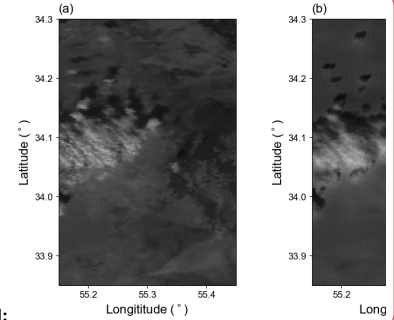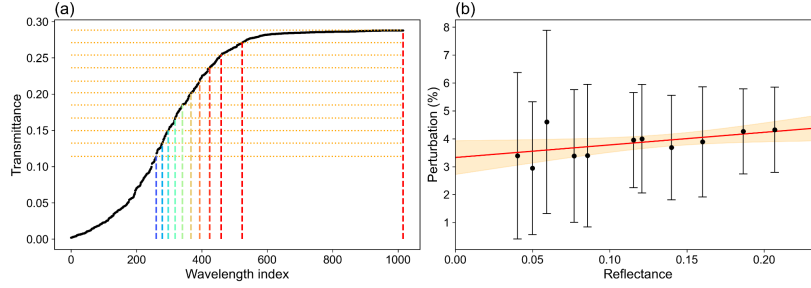
Figure 4: (a) Sorted clear-sky transmittance as per Section 4.2.2, the wavelength index presents the lowest to highest transmittance. (b) Illustration of the selected wavelength distribution in reflectance space versus the Eq. (3) perturbation for 34.08° N, 55.31° E.

5.2. 3D cloud effect parameters analysis

We employed simulated radiance data across three distinct bands to quantify the 3D cloud effect perturbation: s and i. With the horizontal grid cell size around 0.25 km, we derived an approximate mean radiance for a 1 km^2 area by calculating the average radiance of the 5×5 nearest grid points, thereby approximating the OCO-2 footprint. We excluded the data if the 25 nearest grid points contained cloud pixels used in the RT simulation. The distribution of s and i for the O$_2$-A band (s_{O_2-A}, i_{O_2-A}) is illustrated in Fig. 5, with the cloud positions denoted by red dots.
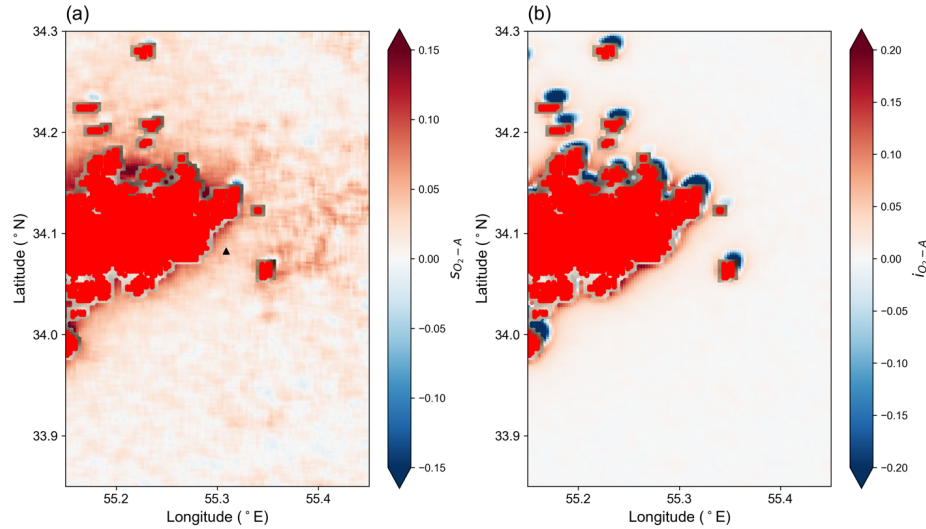
Figure 5: Distribution of (a) s and (b) i of O$_2$-A band. Red dots denote the cloud pixels employed in the RT simulation.

The analysis shows the magnitudes of the 3D cloud effect parameters diminish (s and i get close to 0) as the grid point distance from the cloud increases. This decrease in magnitude corresponds to the smaller 3D cloud effect when the cloud is not in close proximity. Additionally, we divided the clear sky area into two distinct categories: bright and shadow areas. The bright area represents grid points that receive more scattered photons, whereas the shadow area

encompasses grid points within the cloud shadow region. Separating these categories is necessary due to the negative and positive intercepts associated with shadow and bright areas. Notably, both categories exhibit positive s for the three different bands, exhibiting characteristics consistent with those described by Schmidt et al. (2024). Though it is instructive to discuss both cloud brightening and cloud shadowing effects, Massie et al. (2023) determined that there are relatively few cloud shadow retrievals in the OCO-2 Lite files since many observations impacted by shadowing are screened by the OCO-2 pre-retrieval cloud screening algorithms. Thereafter, bright area analyses are the primary focus of our study.

Upon plotting s and i as a function of various definitions of the distance of a given pixel to the surrounding clouds, we identified an exponential decay relationship between the 3D cloud effect parameters and the *effective* horizontal cloud distance (D_e, Fig. 6), which is defined as the average distance of the pixel to the surrounding cloudy pixels, weighted by the inverse square distance to the cloudy pixel (Eq. 5):

$$D_e = \frac{\sum_{i \in \{\text{surrounding clouds}\}} w_i D_i}{\sum_{i \in \{\text{surrounding clouds}\}} w_i} \quad (5)$$

where D_i is the distance of a given pixel to a pixel location of a surrounding cloud, and $w_i = D_i^{-2}$ is the weight. The exponential drop-off shown in Fig. 6 aligns with the result shown in Fig. 6 of Massie et al. (2021), although they used the nearest cloud distance.

The effective cloud distance (D_e) helps minimize the effect of a tiny isolated cloud versus multiple scattered clouds, as displayed in Fig. A4. This exponential decay relationship can be attributed to atmospheric attenuation proportional to their current values. Subsequently, we fitted these parameters and D_e using Eqs. (6)-(7);

$$s = a_s \times \exp(-\frac{D_e}{d_s}) \quad (6)$$

$$i = a_i \times \exp(-\frac{D_e}{d_i}) \quad (7)$$

where amplitude (a_s, a_i) and e-folding distance (d_s, d_i) are the fitting parameters (separate sets for s and i, the slope (s) and intercept (i) parameters that represent the 3D cloud effect). The data are partitioned into multiple columns, employing a bin size of 0.05 reflectance, and we utilize the median of each bin for the fitting procedure. However, we observed that the median s and i values did not approach zero as the cloud distance increased, possibly due to an inadequate number of grid points at larger cloud distances. To rectify this issue, we optimized the fitting coefficients by iteratively increasing the number of points employed in the fitting process until the maximum R^2 value was attained.
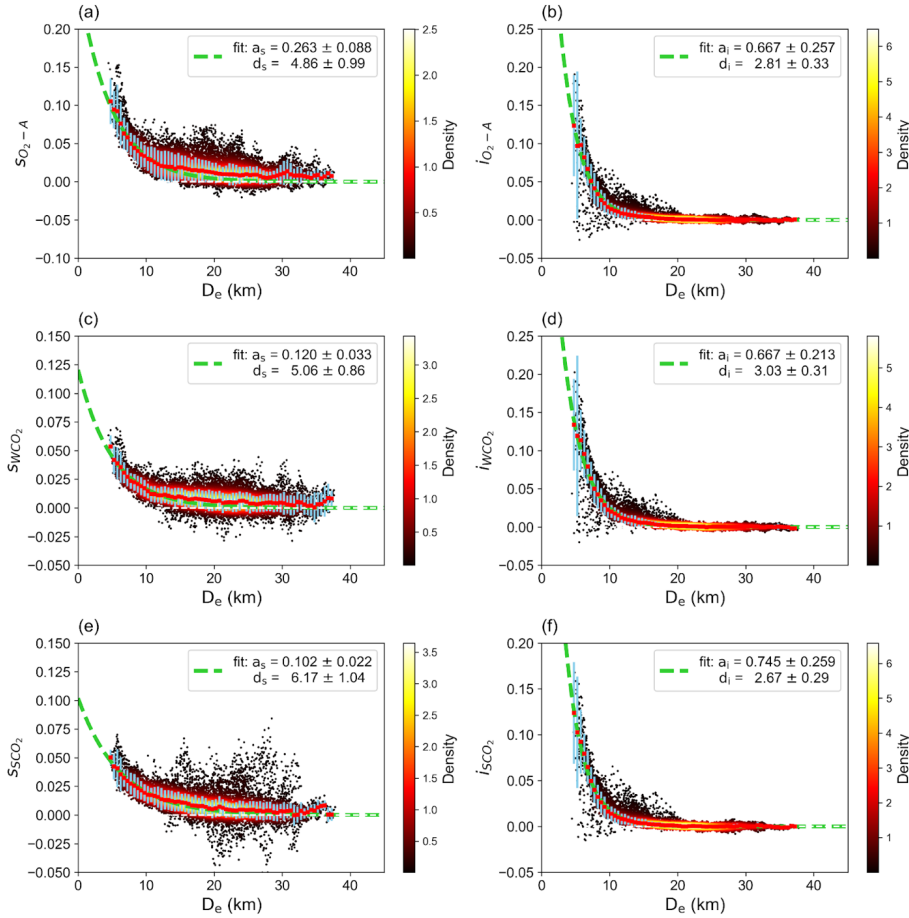
Figure 6: Exponential fitting (green dashed lines) of three bands in the bright area. The black dots present data from each pixel, while the background shading indicates the density of the black dots' distribution. The red points denote the median of each bin, and the blue error bars indicate the first and third quantiles for each bin.

The intercept parameter relates to what is traditionally known as the 3D-RT effect in spectrometry for a wavelength range with minimal gas absorption, whereas the slope is its spectroscopic equivalent, representing spectral distortion due to strongly varying gas absorption cross-sections over a wavelength range. Even slight changes in absorption may result in substantial changes in the retrieved trace gas concentration. The disparity in d_s for each band is not statistically significant, suggesting a similarity in the photon path histories across the different spectral bands.

The initial method, denoted the *baseline method*, applies Eq. (4) on an observation pixel-by-pixel basis and uses only about 1% of the available wavelengths in the three OCO-2 spectra. This method significantly reduces computation time for 3D-RT calculations for a given cloud scene. Next, using the exponential relationships in Eqs. (6)-(7), the 3D
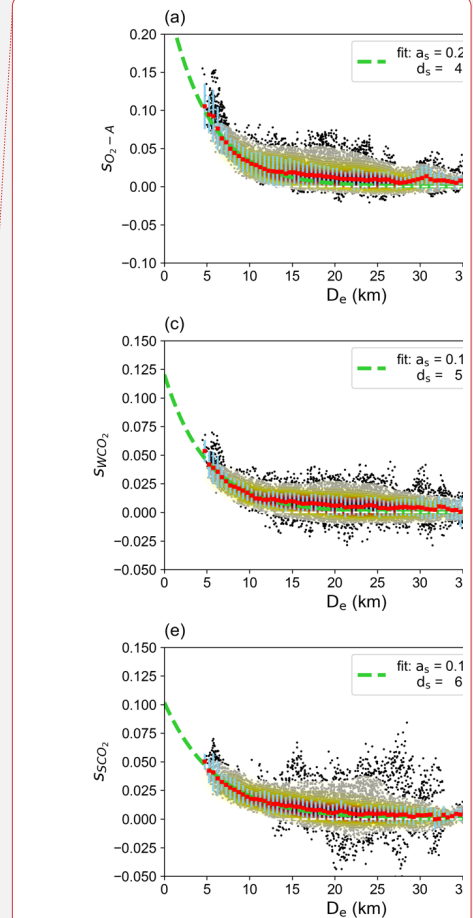
effect can be quantified by determining twelve 3D effect parameters: two amplitudes and two e-folding distances (a_s, d_s and a_i, d_i) for each band. These parameters can be applied to the full scene. Once the effective distance D_e is known for a pixel, the adjusted radiance $I_\lambda^{IPA\,(adjusted)}$ can be readily determined without further 3D-RT simulations (see Section 5.6 for examples). An ensemble of "twelve 3D effect parameters" can be calculated for various cloud spatial distributions, cloud properties, and associated aerosol optical depths. As discussed below in Section 5.5, the twelve 3D effect parameters can be further parameterized in terms of surface albedo and cosine of SZA. This parametric approach will be denoted as the *bypass* method, allowing for evaluating the 3D cloud effect and potentially eliminating the need for 3D-RT simulations altogether.

Table 1. Amplitude and e-folding distances for *s* and *i* fittings in the O$_2$-A, WCO$_2$, and SCO$_2$ bands for the simulation shown in Fig. 5. Errors represent fitting uncertainty only and may be underestimated.

	Slope			Intercept		
	s_{O_2-A}	s_{WCO_2}	s_{SCO_2}	i_{O_2-A}	i_{WCO_2}	i_{SCO_2}
a_s or a_i	0.263 ± 0.088	0.120 ± 0.033	0.102 ± 0.022	0.667 ± 0.257	0.667 ± 0.213	0.745 ± 0.259
d_s or d_i (km)	4.86 ± 0.99	5.06 ± 0.86	6.17 ± 1.04	2.81 ± 0.33	3.03 ± 0.31	2.67 ± 0.29

5.3. Impact of aerosol

Upon establishing the relationship between the 3D cloud effect parameters and the cloud distance, we proceeded to analyze the impact of aerosols on this phenomenon since aerosols play an important role in shortwave radiation. In the presence of aerosols, photons near clouds experience increased extinction (scattering or absorption depending on aerosol radiative properties), making them travel shorter horizontal distances. Consequently, the e-folding distance is expected to be smaller when a higher aerosol loading occurs. To maintain consistency with the previous section, we kept several variables constant, including COT, CER, CTH, cloud position, and atmospheric conditions. However, we introduced a homogeneous aerosol layer into the scenario to investigate its effect on the fitting amplitude and e-folding distance, as detailed in Section 5.2. The aerosol optical depth (AOD) data were obtained from the MODIS MYD04 data file using the aerosol optical depth and angstrom exponent at 550 nm. The top height of the aerosol layer was determined by the prevailing cloud top heights below 4 km, and we assumed uniform AOD values for layers beneath this top height. Aerosol optical depths in the O$_2$-A, WCO$_2$, and SCO$_2$ bands are 0.098, 0.038, and 0.024, respectively.

In the simulation incorporating aerosols, analysis was conducted utilizing the methodology discussed in Section 5.2. Analogous correlations were identified between the 3D cloud parameters and D_e, as shown in Fig. 7 and Table 2. Notably, the presence of an aerosol layer exhibited a pronounced impact on the O$_2$-A and SCO$_2$ bands. This observation aligns with the absorption strength of each spectral band. Consequently, d_s associated with the O$_2$-A and SCO$_2$ bands witness a reduction while a_s of those two bands increases. This suggests that, in the presence of aerosols, the spectral distortion processes within the strong absorption bands are predominantly localized in proximity to the cloud. These findings underscore the pronounced influence of aerosols on the spectral distortion of bands with strong absorptivity.

Note that our simulation relied on the assumption of uniform aerosol distribution within the boundary layer, derived from the mean AOD obtained from the MODIS product. However, this assumption may not always hold true in real-world scenarios. We illustrate that the presence of aerosols can lead to alterations in both the *s* and *i* of the O$_2$-A and SCO$_2$ bands, potentially increasing the uncertainty associated with the derivation of 3D effect parameters.
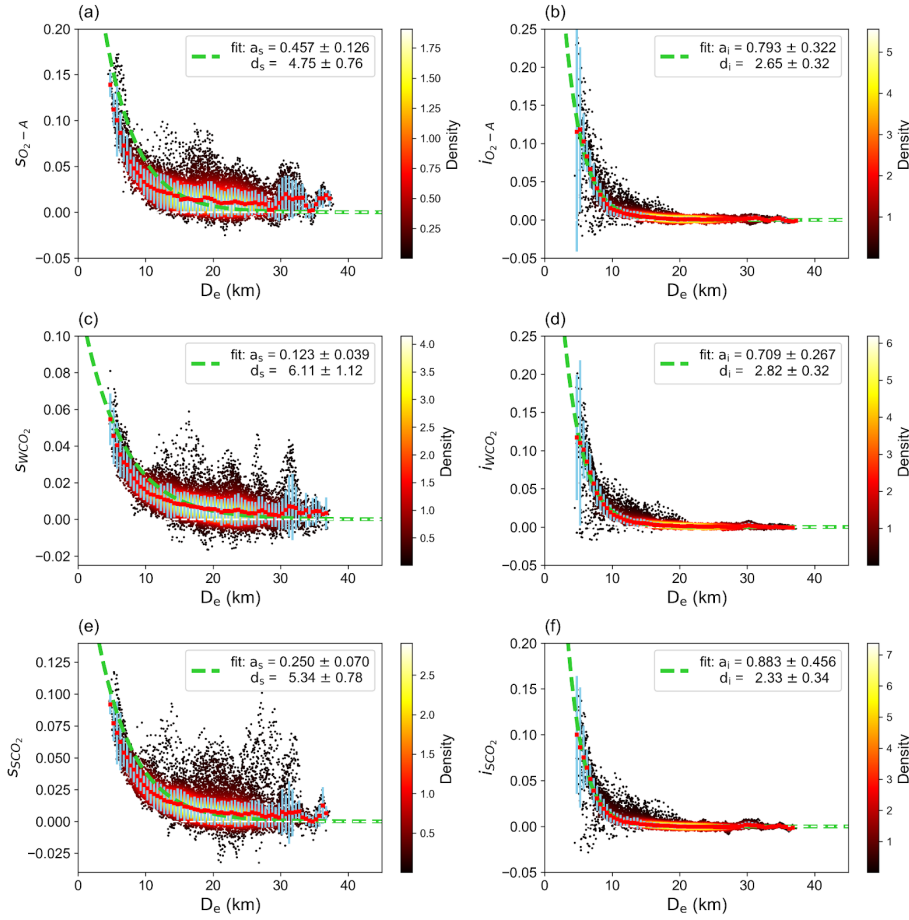
697
698 Figure 7: Exponential fitting (green dashed lines) of the three OCO-2 bands in the bright area of the simulation with
699 a homogeneous aerosol layer. The black dots present data from each pixel, while the background shading indicates
700 the black dots' distribution density. The red points denote the median of each bin, and the blue error bars indicate the
701 first and third quantiles for each bin.

702
703 Table 2. Amplitude and e-folding distances for **s** and **i** fittings of the simulation with a homogeneous aerosol layer in
704 the O_2-A, WCO_2, and SCO_2 bands. Errors represent fitting uncertainty only and may be underestimated.

	Slope			Intercept		
	s_{O_2-A}	s_{WCO_2}	s_{SCO_2}	i_{O_2-A}	i_{WCO_2}	i_{SCO_2}
a_s or a_i	0.457 ± 0.094	0.123 ± 0.037	0.250 ± 0.041	0.755 ± 0.327	0.648 ± 0.227	0.847 ± 0.406
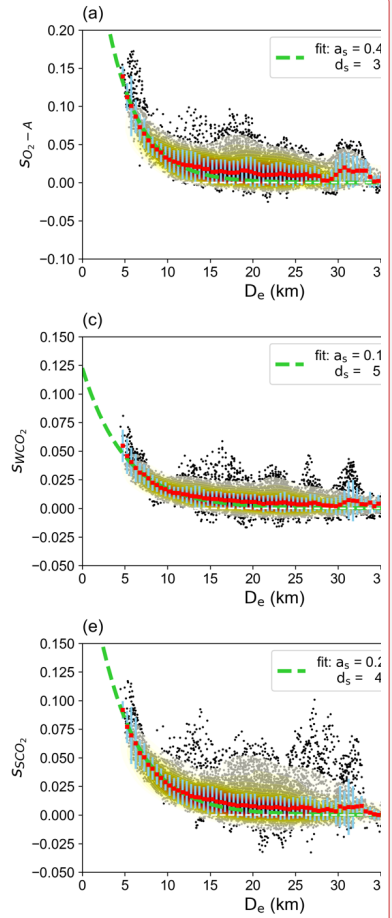
d_s or d_i (km)	3.82 ± 0.44	5.04 ± 0.89	4.58 ± 0.78	2.69 ± 0.32	2.91 ± 0.31	2.35 ± 0.33

Currently, we assume an even distribution of aerosols in the boundary layer in our radiance simulations. However, as Minomura et al. (2001) demonstrate, the effect of aerosols on radiance scattering can vary significantly depending on vertical distribution – mainly when surface albedo differences are pronounced or the aerosol layer is low. In contrast, elevated aerosol layers can extend the horizontal range of adjacency effects, potentially altering the scaling of slope and intercept parameters. This is also applicable to spectroscopy. Consequently, non-uniform vertical aerosol distributions or uncertainties in boundary layer height could introduce variability in evaluating 3D cloud effects. Vertical aerosol and cloud distribution information, such as the data from CALIPSO on the A-train, could be beneficial for improving the accuracy of simulations, but they are not implemented in the initial EaR³T-OCO software release.

5.4. Impact of Footprint Size

Since the OCO instrument series have a narrow field of view (FOV) of 1.3 km × 2.3 km, compared to 78 km² (10.5 km in diameter) for the GOSAT series, the 3D cloud bias is considered more significant for the OCO retrieval when small footprints are in close proximity to clouds. Numerous upcoming satellites for CO₂ remote sensing will adopt similar retrieval algorithms but feature varying footprint sizes in accordance with their specific mission objectives. For example, the Copernicus Anthropogenic CO2 Monitoring Mission (CO2M) by the European Space Agency (ESA) plans to have a footprint size of 4 km² (2 km by 2 km; Kuhlmann et al., 2020). MicroCarb by the Centre National d'Etudes Spatiales (CNES) will have a larger footprint size of 40.5 km² (4.5 km by 9 km; Cansot et al., 2023). Thus, exploring the influence of footprint size on 3D effect parameters is vital. We performed an analysis analogous to the one described in Section 5.3 but expanded the average domain from the closest 5×5 grid points (approximately 1×1 km²) to 9×9, and 13×13 grid points (approximately 2×2, and 3×3 km²). Fig. A5 displays the updated distributions of s and i. The s/i and cloud distance fitting results in the bypass method, presented in Table 3, indicate a decrease in a_s across all three bands. This decline aligns with the expectation that larger footprints would mitigate the spectral distortion effect, reducing the prevalence of the 3D cloud biases. No statistically significant change exists in a_i and d_i in the intercept values across different footprint sizes.

In addition, d_s exhibit an increase compared to the smaller footprint size. This implies that even though the baseline radiance change may demonstrate a minor deviation compared to the 1D-RT simulation as the footprint size expands, the perturbation difference in relation to reflectance might persist due to the increasing d_s. We suggest that future satellite missions, regardless of footprint size, consider accounting for 3D biases to improve the accuracy of X_{CO2} retrievals. Studies need to be conducted to ensure that, given the bands, footprint size, and other attributes, the retrieval error induced by 3D clouds does not exceed the mission requirements – similar to what has been demonstrated for OCO-2 in this study. For missions utilizing larger footprint sizes to achieve broader global coverage, the 3D cloud effect may be diminished but distributed over a more extensive area. Conversely, missions designed with smaller footprint sizes than OCO-2, particularly those targeting enhanced data acquisition in cloud-prone regions such as the Amazon Basin – where Land Nadir observations have been reported to exhibit biases up to -0.48 ppm in both hemispheres (Massie et al., 2023) – must rigorously account for 3D radiative transfer effects. While new missions may propose alternative retrieval algorithms, such as leveraging a reference gas with an absorption band adjacent to the CO₂ band (Frankenberg et al., 2024), these approaches require thorough validation. Therefore, it is imperative that such missions integrate robust 3D-RT mitigation strategies, such as those proposed in Section 5.6, into their design and planning phases to ensure compliance with mission requirements.

Table 3. Amplitude and e-folding distances for s and i, determined using different average grid points in simulations with a homogeneous aerosol layer for the O₂-A, WCO₂, and SCO₂ bands. Errors represent fitting uncertainty only and may be underestimated.

	grid points	Slope	Intercept

		s_{O_2-A}	s_{WCO_2}	s_{SCO_2}	i_{O_2-A}	i_{WCO_2}	i_{SCO_2}
a_s or a_i	1 x 1	0.457 ± 0.094	0.123 ± 0.037	0.250 ± 0.041	0.755 ± 0.327	0.648 ± 0.227	0.847 ± 0.406
	2 x 2	0.355 ± 0.110	0.097 ± 0.025	0.217 ± 0.044	0.758 ± 0.483	0.698 ± 0.360	1.138 ± 0.785
	3 x 3	0.180 ± 0.044	0.079 ± 0.031	0.173 ± 0.058	0.971 ± 0.738	0.922 ± 0.551	1.768 ± 1.548
d_s or d_i (km)	1 x 1	3.82 ± 0.44	5.04 ± 0.89	4.58 ± 0.78	2.69 ± 0.32	2.91 ± 0.31	2.35 ± 0.33
	2 x 2	4.24 ± 0.68	5.82 ± 0.95	4.94 ± 0.62	2.61 ± 0.45	2.78 ± 0.40	2.16 ± 0.36
	3 x 3	6.20 ± 1.03	6.46 ± 1.57	5.46 ± 1.07	2.47 ± 0.46	2.61 ± 0.40	2.00 ± 0.36

5.5.   Impact of Solar Zenith Angle and Surface Reflectance

Solar zenith angle and surface albedo are significant factors influencing the 3D cloud effect, represented by a parameterized set of 12 relationships. To investigate their impact on the 3D cloud effect, we also kept several variables constant, including COT, CER, CTH, cloud position, AOD, and atmospheric conditions, as the setup used in Section 5.3, and manually changed the SZA and surface reflectance. Figures A5 and A6 illustrate how these variables impact the 3D cloud effect in the O_2-A band under different conditions. Combining results across various solar zenith angles and surface albedo values, we developed a two-variable linear parameterization using a_s and d_s (slope parameters) and a_i and d_i (intercept parameters). As summarized in Table 4, we observe that the amplitude of the slope and intercept is inversely proportional to surface albedo and directly proportional to the cosine of the solar zenith angle (denoted as μ). Additionally, the e-folding distances of the slope (d_s) and are negatively proportional to both surface albedo and μ, while those of the intercept are positively proportional to surface albedo and negatively proportional to μ. In general, higher surface albedo reduces the 3D cloud effect, as additional photons reaching the sensor represent a smaller fraction of the total signal. Conversely, lower solar zenith angles result in a smaller amplitude but longer e-folding distance, causing the 3D effect to extend further from the clouds.

Table 4. The parameterization of a_s and d_s of slope and a_i and d_i of intercept for the three OCO-2 bands. Errors represent fitting uncertainty only and may be underestimated.

	slope	intercept
O_2-A	$a_s = -0.34 \times \text{albo}_{2\text{-A}} + 0.57 \times \mu - 0.03$ $d_s = -3.2 \times \text{albo}_{2\text{-A}} - 9.9 \times \mu + 14.9$	$a_i = -0.60 \times \text{albo}_{2\text{-A}} + 0.36 \times \mu + 0.72$ $d_i = 0.42 \times \text{albo}_{2\text{-A}} - 2.1 \times \mu + 5.2$
WCO_2	$a_s = -0.15 \times \text{alb}_{WCO2} + 0.11 \times \mu - 0.05$ $d_s = -30.7 \times \text{alb}_{WCO2} - 7.0 \times \mu + 27.5$	$a_i = -2.07 \times \text{alb}_{WCO2} + 1.65 \times \mu + 1.17$ $d_i = 0.63 \times \text{alb}_{WCO2} - 1.6 \times \mu + 3.7$
SCO_2	$a_s = -0.18 \times \text{alb}_{SCO2} + 0.29 \times \mu - 0.03$ $d_s = -22.6 \times \text{alb}_{SCO2} - 21.2 \times \mu + 34.9$	$a_i = -2.77 \times \text{alb}_{SCO2} + 2.22 \times \mu + 1.14$ $d_i = 0.51 \times \text{alb}_{SCO2} - 1.73 \times \mu + 3.35$

5.6.   3D effect mitigation

Utilizing the derived **s** and **i** for the 3D effect, we can mitigate the associated biases through the "radiance adjustment" process, as elaborated in Section 4.4. The assumption is that the 3D effect is removed in the adjusted 1D radiance, allowing us to retrieve the mitigated X_{CO2} using existing operational retrieval algorithms. To mitigate the 3D biases in X_{CO2}, it is essential to compute the 3D parameters (**s** and **i** for the three OCO-2 spectral bands) for all footprints that pass the pre-screening (Quality Flag = 0 or 1).

Deleted: the 3D effect

794 Both the *baseline* and *bypass* methods rely on the same mitigation framework but differ in how s and i are
795 obtained for each footprint. In the baseline method, 3D-RT simulations are performed on a per-pixel basis to directly
796 obtain s and i. By contrast, the bypass method first calculates D_e for each footprint based on the cloud position,
797 incorporating parallax and wind correction (refer to Fig. A4 as an example), and then uses exponential-fit coefficients
798 in Table 2 to map D_e to s and i. Finally, the adjusted spectra are derived for both methods in accordance with Eq. (4).
799 Fig. 8 presents an example of the original and corresponding adjusted spectra of the O_2-A band. In this study, we
800 demonstrate the integration of our mitigation framework into current operational retrieval algorithms to effectively
801 reduce the 3D cloud bias.
802
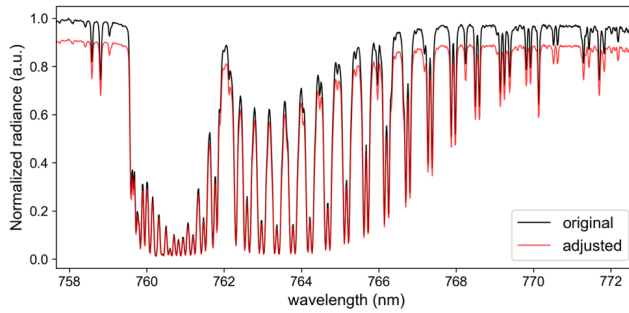
803
804 Figure 8: Example of an O_2-A spectrum before and after radiance adjustment.

805 Using the B10.04 retrieval algorithm (refer to Section 4.4), we calculate the newly retrieved X_{CO2} values for each
806 footprint. Fig. 9 displays the distribution of retrieved X_{CO2} before and after the spectral adjustment, superimposed on
807 the collocated MODIS Aqua image. The elevated X_{CO2} near the cloud decreases after the adjustment approximation,
808 with the newly retrieved X_{CO2} values reduced by approximately 0 to 3 ppm for D_e greater than 5 km and by more than
809 3 ppm for D_e less than 5 km. A comparison of ΔX_{CO2} (the newly retrieved X_{CO2} minus the original L2 value) against
810 D_e is presented in Fig. 10 for both methods. Both methods exhibit analogous ΔX_{CO2} patterns and offer similar average
811 reductions. Specifically, the bypass method registers an average ΔX_{CO2} of -0.778 ppm, in contrast to the baseline
812 method, which delineates an average ΔX_{CO2} of -0.876 ppm. The observed variance of ΔX_{CO2} potentially emanates
813 from simplified assumptions in the bypass method. Larger biases near cloud edges are captured more accurately by
814 the baseline method, but both approaches confirm that the bias diminishes with increasing cloud distance.
815

816
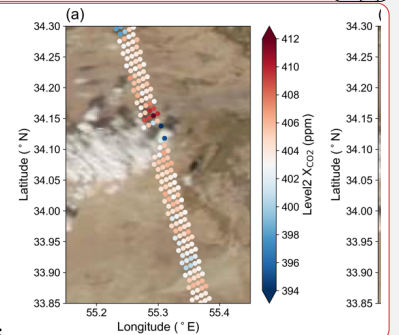
Figure 9: Satellite true-color imagery of MODIS Aqua from NASA Worldview on 18 October 2018 with (a) X_{CO2} in
OCO-2 level 2 data, (b) mitigated X_{CO2} retrieved from the adjusted spectra and (c) difference between the mitigated
and original X_{CO2} values.
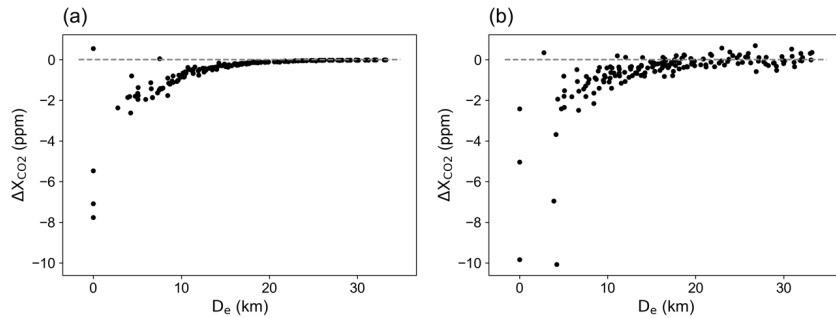
Figure 10: (a) Relationship of ΔX_{CO2} with D_e as depicted in Fig. 7c, based on parameterized slopes and intercepts
from the bypass method. ΔX_{CO2} is defined as the difference between the newly retrieved X_{CO2} and level 2 X_{CO2}. (b)
Corresponding relationship using slopes and intercepts derived from the baseline approach.

The requirement of the OCO-2 mission is to determine X_{CO2} uncertainty to within 1 ppm. Setting the true
mixing ratio to the mean X_{CO2} for an effective distance exceeding 15 km, we see that X_{CO2} scatter is accentuated within
15 km of clouds, as demarcated by the black markers in Fig. 11a. The mitigated X_{CO2} after the spectra adjustment,
represented by the red markers in Fig. 11a, exhibits reduced scatter within 15 km of clouds, a fact further corroborated
by the full width at half maximum (FWHM) depicted in Fig. 11b. Cumulatively, the bypass method aligns favorably
with the baseline methodology, offering the added benefit of small computational demands. Our physically based
adjustment thus achieves the 3D bias reduction near clouds at radiance level for the first time while still allowing the
use of the original 1D retrieval code.

The processing time per footprint for baseline analysis is approximately 7 minutes when using 32 CPUs
(AMD EPYC Processor 7713) on a cluster to simulate 1×10^9 photons for the full experiment domain. This is
contrasted with the standard retrieval time of roughly 2.5 minutes per footprint using 16 CPUs (Intel Xeon Processor
E5-2623 v3) on a local workstation. Although the 3D computation time of 7 minutes marks a significant improvement
over full-spectra 3D simulation, the additional 3D-RT calculations required to account for the missing physics could
extend the duration to nearly 6 times that of standard retrieval on a per-footprint, per-CPU basis. The bypass method
offers a pragmatic alternative to mitigating the 3D cloud effect for large-scale applications while conserving
computational resources. This method can be supplemented by periodic full calculations to increase the accuracy of
the bypass approach but needs to be tested on a larger dataset before further application.

Deleted: The observed variance of X_{CO2} potentially
emanates from the oversimplification of the 3D cloud effect
by the current bypass method, which predominantly draws
from brightening regions. Nikolaeva et al. (2005) classified
the 3D cloud effect into four distinct types (brightening,
shadowing, photons channeling, and photons leaking), with
only the brightening effect being investigated in this study.
The shadow area, which is not the primary focus of this
research, also contributes to X_{CO2} retrieval biases. The
existing bypass method cannot mitigate these biases and may
even be exacerbated after the adjustment. Moreover, specific
footprints containing thin clouds that pass the cloud-
screening test also exhibit X_{CO2} retrieval biases. Such
footprints, near the cloud periphery or partially
encompassing the cloud, might not be optimal candidates for
the parameterization (i.e. bypass) technique. ¶

Deleted: Concurrently, our proposed mitigation method
could integrate into the current retrieval system, which
deploys the 1D-RT model by introducing it as a
preprocessing step and effectively diminishes the impact of
the 3D effect at the footprint level for the first time. The next
step in this process is to test this methodology on a larger
dataset.

Deleted: at the University of Colorado

Deleted: Such a duration is impractical in operational
settings. Therefore, o

Deleted: ur
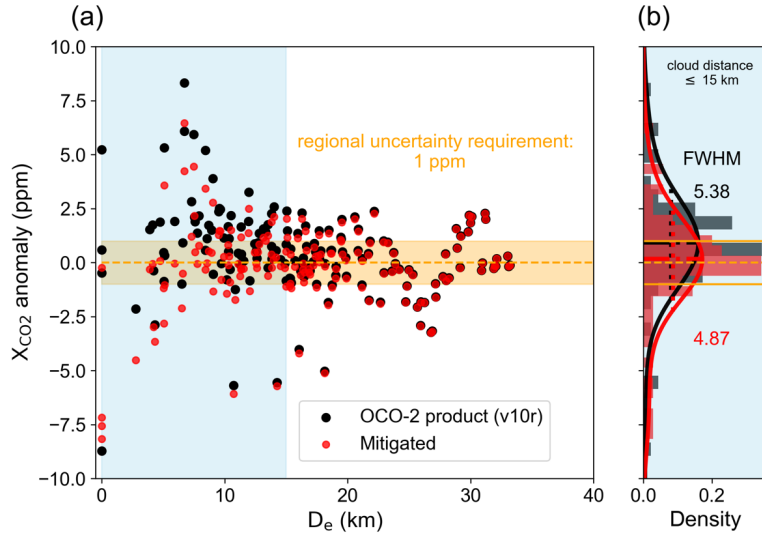
Figure 11: (a) Scatter plot comparing the X_{CO2} anomaly of the OCO-2 L2 product (in black) to its value post-spectra adjustment (in red), plotted against D_e. The X_{CO2} anomaly is defined as retrieved X_{CO2} – true X_{CO2}, with the true X_{CO2} defined by the average X_{CO2} of footprints with a D_e greater than 15 km (403.714 ppm in this case). The orange shade indicates the 1 ppm mission requirement. (b) Histograms and probability density functions (PDFs) for the X_{CO2} anomaly of the OCO-2 L2 product (in black) and post-spectra adjustment (in red) within a 15 km D_e. This corresponds to the blue-shaded region in (a). The FWHM values of the PDFs of v10r and adjusted data points are 5.38 and 4.87, and the PDF averages are 0.796 and -0.178, respectively. The average change in X_{CO2} after the spectra adjustment for De less than 15 km is -1.131 ppm.

To evaluate the applicability of the bypass approach, we applied the parameter set in Table 2 to another scene (Fig. A7a) from the same month and nearby region. We also conducted a baseline 3D-RT simulation for direct comparison (Fig. A8). The results indicate that the bypass method follows a trend similar to the baseline method, although with smaller mitigation magnitudes. Differences between the two (Fig. 9) are likely due to variations in surface altitude, albedo, solar geometry, AOD, and other factors. Although promising, the bypass approach may benefit from additional tuning to account for these scene variables. However, it can be less effective under complex cloud-surface conditions.

6. Conclusions

This research uses the EaR³T-OCO radiance simulator, which considers the scene context of givens, to evaluate and mitigate the impact of missing physics in the context-agnostic operational retrieval that stems from clouds in the vicinity of an OCO-2 sounding. We then used the simulator to undo the effects of such clouds by reversing the perturbations relative to the clear sky that they exert on the observed radiances. In essence, the observed radiance spectra were mapped back to what they *would have been* in the *absence* of clouds in the vicinity of a footprint. This radiance mapping is done based on the difference between simulated 1D and 3D radiance calculations (3D

perturbations). After this mapping, the standard X_{CO_2} retrieval can then be applied. In this way, we introduced a physics-based mitigation of 3D-RT effects on trace gas spectroscopy products, previously regarded as intractable for real-world applications such as this.

To avoid 'brute-force' computing full-spectrum 3D effects, we introduced a physics-based acceleration approach with only a few representative wavelengths. The resulting 3D perturbations are encapsulated by twelve linear fit parameters (slope and offset), reducing the complexity of the correction. This acceleration method is distinct from previously published methods, including approaches to "freeze" photon paths for various wavelengths (Emde et al., 2011, Iwabuchi and Okamura, 2017). The spectral perturbation parameters can also be linked to macroscopic scene parameters to analyze their influence on 3D cloud effects. If successful, this method could bypass 3D-RT calculations altogether while retaining the core physics. By applying this bypass parameterization approach, the mitigation of cloud effects at the radiance level becomes feasible for operational applications, offering a stronger physical foundation compared to statistical mitigation methods and enabling broad applicability to OCO-2/3 and other spectroscopy missions that have collocated imagery.

Although further validation is required for a wider diversity of scenes, including variations in cloud top height, cloud morphology, aerosols, and different viewing modes, the linear perturbation representation and our mitigation framework approach account for the principal drivers of 3D cloud effects. Moreover, it highlights that aerosols and footprint size can influence the magnitude of the 3D cloud effect, especially for future satellites such as MicroCarb, CO2M, and GOSAT-GW. In general, our research elucidates the 3D cloud perturbation on *spectroscopy* with high spectral resolution (trace gas retrievals) as opposed to *spectrometry* (cloud and aerosol imagery retrievals), where 3D effects are traditionally studied more extensively. Addressing these effects at the radiance level is suggested because that is where the operational standard 1D retrievals lack the necessary physics. We also understand that the effects are spectrally dependent, with cloud morphology, band-specific surface reflectance, and aerosol properties acting as the primary drivers. Our work can become the stepping stone toward more accurate and efficient trace gas retrievals in the vicinity of clouds. Looking ahead, adapting this mitigation to operational workflows could markedly improve X_{CO_2} accuracy in cloud-prone regions—including the Amazon—and thereby enhance the fidelity of CO_2 flux inversions.

7.   Future work

This research emphasizes the substantial impact of aerosols, solar zenith angles, and surface albedo on the 3D effect parameters of the three OCO bands. Concurrently, cloud properties emerge as critical determinants of these 3D effect parameters. With additional simulations, there is an opportunity to incorporate the impacts of various factors into the existing parameterization framework. The current investigation concentrates on scenarios over land in Nadir mode. We will develop a similar parameterization (as in Table 3) for ocean and land in Glint mode.

Code availability

The EaR³T code (Chen et al., 2023) is available at https://github.com/hong-chen/er3t, and the EaR³T-OCO code is available at https://github.com/ywchen-tw/OCO2

Data availability

Version 10r of OCO-2 data can be accessed at https://oco2.gesdisc.eosdis.nasa.gov/data/OCO2_DATA. The MODIS-related data from data collection 6.1, including MYD02QKM, MYD02HKM, MYD021KM, MYD03, MYD06, MYD04_L2, and MCD43A3, are available at https://ladsweb.modaps.eosdis.nasa.gov/. We acknowledge the use of

1136 imagery from the Worldview Snapshots application (https://wvs.earthdata.nasa.gov), part of the Earth Observing
1137 System Data and Information System (EOSDIS).

Author contribution

1139 YWC and SS developed the conceptual framework of the presented methodology. YWC was primarily responsible
1140 for carrying out the radiance simulations and analyzing the data. HC played a supporting role in the development of
1141 the EaR^{3}T-OCO program. All authors worked collaboratively to refine the methods, deliberate over the results, and
1142 contribute to drafting the original manuscript.

Competing interests

1144 At least one of the (co-)authors is a member of the editorial board of Atmospheric Measurement Techniques.

Financial support

1146 This research has greatly benefited from the insights and resources provided by two ROSES projects, "Reducing
1147 OCO-2 regional biases through novel 3D cloud, albedo, and meteorology estimation", 20-OCOST20-0031, Susan
1148 Kulawik, PI; and "Mitigation of 3D Cloud Radiative Effects in OCO-2 and OCO-3 XCO2 Retrievals,"
1149 80NSSC21K1063, Steven Massie, PI. We also extend our appreciation to the National Aeronautics and Space
1150 Administration (grant no. 80NSSC18K0146) for developing EaR^{3}T. This work utilized the Alpine high performance
1151 computing resource at the University of Colorado Boulder. Alpine is jointly funded by the University of Colorado
1152 Boulder, the University of Colorado Anschutz, Colorado State University, and the National Science Foundation
1153 (award 2201538).

Abbreviations

1155 The following abbreviations are used in this manuscript:

A-train	Earth Observing System Afternoon Constellation
ABSCO	Absorption coefficients
AOD	Aerosol optical depth
CER	Cloud effective radius
CO_2	Carbon dioxide
COT	Cloud optical thickness
CTH	Cloud top height
EaR^{3}T	Education and Research 3D Radiative Transfer Toolbox
FOV	Field of view
FWHM	Full Width at Half Maximum
GMAO	Global Modeling Assimilation Office

GOSAT	Greenhouse Gases Observing Satellite
L (0,1..)	Level 0, Level 1, etc. (data product)
MCARaTS	Monte Carlo Atmospheric Radiative Transfer Simulator
MODIS	Moderate-Resolution Imaging Spectroradiometer
O_2-A	Oxygen A-band
OCO	Orbiting Carbon Observatory
ppm	parts per million
R^2	Determination coefficient
RT	Radiative transfer
SCO_2	Strong CO_2
SZA	Solar zenith angle
TOA	Top of atmosphere
VMR	Volume mixing ratio
WCO_2	Weak CO_2
X_{CO2}	Column-averaged CO_2 dry air mole fraction

1162

References

Bosilovich, M.G., Lucchesi, R. and Suarez, M.: MERRA-2: File specification, No. GSFC-E-DAA-TN27096, 2015.

Chen, H., Schmidt, K. S., Massie, S. T., Nataraja, V., Norgren, M. S., Gristey, J. J., Feingold, G., Holz, R. E., and Iwabuchi, H: The Education and Research 3D Radiative Transfer Toolbox (EaR^{3}T) – towards the mitigation of 3D bias in airborne and spaceborne passive imagery cloud retrievals, Atmos. Meas. Tech., 16, 1971–2000, https://doi.org/10.5194/amt-16-1971-2023, 2023.

Cansot, E., Pistre, L., Castelnau, M., Landiech, P., Georges, L., Gaeremynck, Y., and Bernard P.: MicroCarb instrument, overview and first results, Proc. SPIE 12777, International Conference on Space Optics — ICSO 2022, 1277734 (12 July 2023); https://doi.org/10.1117/12.269033.

Connor, B., and Coauthors: Quantification of uncertainties in OCO-2 measurements of XCO2: simulations and linear error analysis, Atmos. Meas. Tech., 9, 5227–5238, https://doi.org/10.5194/amt-9-5227-2016, 2016.

Crisp, D.: September. Measuring atmospheric carbon dioxide from space with the Orbiting Carbon Observatory-2 (OCO-2), Proc. SPIE 9607, Earth Observing Systems XX, 960702, https://doi.org/10.1117/12.2187291, 2015.

Crowell, S. M. R., Randolph Kawa, S., Browell, E. V., Hammerling, D. M., Moore, B., Schaefer, K., and Doney, S. C., 2018: On the ability of space-based passive and active remote sensing observations of CO2 to detect flux perturbations to the carbon cycle, J. Geophys. Res.-Atmos., 123, 1460–1477.

Deng, F., D. B. A. Jones, C. W. O'Dell, R. Nassar, and N. C. Parazoo, 2016: Combining GOSAT XCO2 observations over land and ocean to improve regional CO2 flux estimates, J. Geophys. Res.-Atmos., 121, 1896–1913.

Doicu, A., Efremenko, D.S., Trautmann, T., 2020: A Spectral Acceleration Approach for the Spherical Harmonics Discrete Ordinate Method, Remote Sens., 2020, 12, 3703. https://doi.org/10.3390/rs12223703, 2020.

Eldering, A., Taylor, T.E., O'Dell, C.W. and Pavlick, R.: The OCO-3 mission: measurement objectives and expected performance based on 1 year of simulated data, Atmos. Meas. Tech., 12, 2341-2370, https://doi.org/10.5194/amt-12-2341-2019, 2019.

Emde, C., Buras, R. and Mayer, B.: ALIS: An efficient method to compute high spectral resolution polarized solar

1188   radiances using the Monte Carlo approach, J. Quant. Spectrosc. Ra., 112,1622-1631,
1189   https://doi.org/10.1016/j.jqsrt.2011.03.018, 2011.
1190 Frankenberg, C., Bar-On, Y.M., Yin, Y., Wenberg, P.O., Jacob, D.J. and Michalak, A.M.: Data Drought in the Humid
1191   Tropics: How to Overcome the Cloud Barrier in Greenhouse Gas Remote Sensing, ESS Open Archive
1192   [preprint], https://doi.org/10.22541/essoar.170923255.57545328/v1, 29 February 2024.
1193 Frey, R. A., Ackerman, S. A., Holz, R. E., Dutcher, S. and Griffith, Z.: The Continuity MODIS-VIIRS Cloud Mask,
1194   Remote Sens., 12, 3334, https://doi.org/10.3390/rs12203334, 2020.
1195 Imasu, R., Matsunaga, T., Nakajima, M., Yoshida, Y., Shiomi, K., Morino, I., Saitoh, N., Niwa, Y., Someya, Y., Oishi,
1196   Y. and Hashimoto, M.: Greenhouse gases Observing SATellite 2 (GOSAT-2): mission overview, Prog. Earth
1197   Planet Sci., 10, 33, https://doi.org/10.1186/s40645-023-00562-2, 2023.
1198 Iwabuchi, H.: Efficient Monte Carlo Methods for Radiative Transfer Modeling, J. Atmos. Sci., 63, 2324–2339,
1199   https://doi.org/10.1175/JAS3755.1, 2006.
1200 Iwabuchi, H. and Okamura, R.: Multispectral Monte Carlo radiative transfer simulation by the maximum cross-section
1201   method, J. Quant. Spectrosc. Ra., 193, 40-46, https://doi.org/10.1016/j.jqsrt.2017.01.025, 2017.
1202 King, M. D., S. Platnick, W. P. Menzel, S. A. Ackerman, and P. A. Hubanks: Spatial and Temporal Distribution of
1203   Clouds Observed by MODIS Onboard the Terra and Aqua Satellites, IEEE Trans. Geosci. Remote Sens., 51,
1204   3826–3852, https://doi.org/10.1109/TGRS.2012.2227333, 2013.
1205 Kylling, A., C. Emde, H. Yu, M. van Roozendael, K. Stebel, B. Veihelmann, and B. Mayer: Impact of 3D cloud
1206   structures on the atmospheric trace gas products from UV–Vis sounders – Part 3: Bias estimate using
1207   synthetic and observational data, Atmos. Meas. Tech., 15, 3481–3495, https://doi.org/10.5194/amt-15-3481-
1208   2022, 2022.
1209 Kuhlmann, G., Brunner, D., Broquet, G., and Meijer, Y.: Quantifying CO2 emissions of a city with the Copernicus
1210   Anthropogenic CO2 Monitoring satellite mission, Atmos. Meas. Tech., 13, 6733–6754,
1211   https://doi.org/10.5194/amt-13-6733-2020, 2020.
1212 Li, S. and Yang, J., 2024: Retrieving global single-layer liquid cloud thickness from OCO-2 hyperspectral oxygen A-
1213   band, Remote Sens. Envrion., 311, 113272, https://doi.org/10.1016/j.rse.2024.114272.
1214 Levy, R. and Hsu, C.: MODIS Atmosphere L2 Aerosol Product. NASA MODIS Adaptive Processing System,
1215   Goddard Space Flight Center, USA [Data set]: http://dx.doi.org/10.5067/MODIS/MYD04_L2.061, 2015.
1216 Mauceri, S., Massie, S., and Schmidt, S.: Correcting 3D cloud effects in XCO2 retrievals from the Orbiting Carbon
1217   Observatory-2 (OCO-2), Atmos. Meas. Tech., 16, 1461–1476, https://doi.org/10.5194/amt-16-1461-2023,
1218   2023.
1219 Massie, S. T., K. Sebastian Schmidt, A. Eldering, and D. Crisp: Observational evidence of 3-D cloud effects in OCO-
1220   2 CO2 retrievals, J. Geophys. Res.-Atmos., 122, 7064–7085, https://doi.org/10.1002/2016JD026111, 2017.
1221 Massie, S. T., Cronk, H., Merrelli, A., O'Dell, C., Schmidt, K. S., Chen, H., and Baker, D.: Analysis of 3D cloud
1222   effects in OCO-2 XCO2 retrievals, Atmos. Meas. Tech., 14, 1475–1499, https://doi.org/10.5194/amt-14-
1223   1475-2021, 2021.
1224 Massie, S., Cronk, H., Merrelli, A., Schmidt, S., & Mauceri, S.: Insights into 3D cloud radiative transfer effects for
1225   the Orbiting Carbon Observatory, Atmos. Meas. Tech., 16, 2145–2166, https://doi.org/10.5194/amt-16-
1226   2145-2023, 2023.
1227 Miller, C. E., Crisp, D., DeCola, P. L., Olsen, S. C., Randerson, J. T., Michalak, A. M., Alkhaled, A., Rayner, P.,
1228   Jacob, D. J., Suntharalingam, P., Jones, D. B. A., Denning, A. S., Nicholls, M. E., Doney, S. C., Pawson, S.,
1229   Boesch, H., Connor, B. J., Fung, I. Y., O'Brien, D., Salawitch, R. J., Sander, S. P., Sen, B., Tans, P., Toon,
1230   G. C., Wennberg, P. O., Wofsy, S. C., Yung, Y. L., and Law, R. M.: Precision requirements for space-based
1231 X_{CO2} data, J. Geophys. Res.-Atmos., 112, D10314, https://doi.org/10.1029/2006JD007659, 2007.
1232 Minomura, M., KUzE, H. and Takeuchi, N., 2001: Adjacency effect in the atmospheric correction of satellite remote
1233   sensing data: Evaluation of the influence of aerosol extinction profiles. Optical review, 8, 133-141,
1234   https://doi.org/10.1007/s10043-0010133-2, 2001.
1235 MODIS Characterization Support Team (MCST): MODIS 1km Calibrated Radiances Product, NASA MODIS
1236   Adaptive Processing System, Goddard Space Flight Center, USA [Data set],
1237   http://dx.doi.org/10.5067/MODIS/MYD021KM.061, 2017.
1238 MODIS Characterization Support Team (MCST): MODIS 250m Calibrated Radiances Product, NASA MODIS
1239   Adaptive Processing System, Goddard Space Flight Center, USA [Data set],
1240   http://dx.doi.org/10.5067/MODIS/MYD02QKM.061, 2017.
1241 MODIS Characterization Support Team (MCST): MODIS 500m Calibrated Radiance Product, NASA MODIS
1242   Adaptive Processing System, Goddard Space Flight Center, USA [Data set]:
1243   http://dx.doi.org/10.5067/MODIS/MYD0HKM.061, 2017.

1244 MODIS Characterization Support Team (MCST): MODIS Geolocation Fields Product. NASA MODIS Adaptive
1245   Processing System, Goddard Space Flight Center, USA [Data set],
1246   http://dx.doi.org/10.5067/MODIS/MYD03.061, 2017.
1247 Nakajima, M., Kuze, A., Kawakami, S., Shiomi, K. and Suto, H.: Monitoring of the greenhouse gases from space by
1248   GOSAT, Int. Arch. Photogramm., 38, 94-99, 2010.
1249 Nelson, R. R., J. McDuffie, S. S. Kulawik, and C. O'Dell: Water and Temperature SVD Estimates to Improve OCO-
1250   2 XCO2 Errors, AGU Fall Meeting Abstracts, Chicago, USA, 12-16 Dec. 2022, A15L-1402, 2022.
1251 O'Dell, C. W., Eldering, A., Wennberg, P. O., Crisp, D., Gunson, M. R., Fisher, B., Frankenberg, C., Kiel, M.,
1252   Lindqvist, H., Mandrake, L., Merrelli, A., Natraj, V., Nelson, R. R., Osterman, G. B., Payne, V. H., Taylor,
1253   T. E., Wunch, D., Drouin, B. J., Oyafuso, F., Chang, A., McDuffie, J., Smyth, M., Baker, D. F., Basu, S.,
1254   Chevallier, F., Crowell, S. M. R., Feng, L., Palmer, P. I., Dubey, M., García, O. E., Griffith, D. W. T., Hase,
1255   F., Iraci, L. T., Kivi, R., Morino, I., Notholt, J., Ohyama, H., Petri, C., Roehl, C. M., Sha, M. K., Strong, K.,
1256   Sussmann, R., Te, Y., Uchino, O., and Velazco, V. A.: Improved retrievals of carbon dioxide from Orbiting
1257   Carbon Observatory-2 with the version 8 ACOS algorithm, Atmos. Meas. Tech., 11, 6539–6576,
1258   https://doi.org/10.5194/amt-11-6539-2018, 2018.
1259 Payne, V. H., and Coauthors, 2020: Absorption coefficient (ABSCO) tables for the Orbiting Carbon Observatories:
1260   Version 5.1, J. Quant. Spectrosc. Radiat. Transf., 255, 107217, https://doi.org/10.1016/j.jqsrt.2020.107217.
1261 Rodgers, C.D., 2000: Inverse methods for atmospheric sounding: theory and practice (Vol. 2). World Scientific.
1262 Várnai, T., and A. Marshak, 2009: MODIS observations of enhanced clear sky reflectance near clouds, Geophys. Res.
1263   Lett., 36, https://doi.org/10.1029/2008GL037089.
1264 Worden, J. R., G. Doran, S. Kulawik, A. Eldering, D. Crisp, C. Frankenberg, C. O'Dell, and K. Bowman, 2017:
1265   Evaluation and attribution of OCO-2 XCO$_2$ uncertainties, Atmos. Meas. Tech., 10, 2759–2771,
1266   https://doi.org/10.5194/amt-10-2759-2017.
1267 Wylie, D., D. L. Jackson, W. P. Menzel, and J. J. Bates, 2005: Trends in Global Cloud Cover in Two Decades of HIRS
1268   Observations, J. Clim., 18, 3021–3031, https://doi.org/10.1175/JCLI3461.1.
1269 OCO-2 L1B ATBD: Orbiting Carbon Observatory-2 & 3 (OCO-2 & OCO-3) Level 1B Algorithm Theoretical Basis,
1270   Version 2.0 Rev 0, January 15, JPL, California Institute of Technology, Pasadena, California, USA, 2021.
1271 OCO-2 L2 ATBD: Orbiting Carbon Observatory-2 & 3 (OCO-2 & OCO-3) Level 2 Full Physics Retrieval Algorithm
1272   Theoretical Basis, Version 2.0 Rev 3 January 2, JPL, California Institute of Technology, Pasadena, California,
1273   USA, 2020.
1274 Partain, P. T., A. K. Heidinger, and G. L. Stephens, 2000: High spectral resolution atmospheric radiative transfer:
1275   Application of the equivalence theorem, J. Geophys. Res., 105, 21632177, doi:10.1029/1999JD900328, 2000.
1276 Platnick, S., Ackerman, S., King, M., Meyer, K., Menzel, W.P., Holz, R.E., Baum, B.A. and Yang, P.J.N.M.A.P.S.:
1277   MODIS Atmosphere L2 Cloud Product (06_L2), NASA MODIS Adaptive Processing System, Goddard
1278   Space Flight Center, USA [Data set], http://dx.doi.org/10.5067/MODIS/MOD06_L2.061, 2015.
1279 Schaaf, C. and Wang, Z.: MODIS/Terra+Aqua BRDF/Albedo Daily L3 Global - 500m V061, NASA EOSDIS Land
1280   Processes Distributed Active Archive Center [Data set], https://doi.org/10.5067/MODIS/MCD43A3.061,
1281   2021.
1282 Schmidt, K. S., Massie, S., and Feingold, G., 2019: Impact of Broken Clouds on Trace Gas Spectroscopy From Low
1283   Earth Orbit. In Hyperspectral Imaging and Sounding of the Environment (Optica Publishing Group, 2019),
1284   paper HW5C-2.
1285 University of Colorado Boulder Research Computing, Alpine, University of Colorado Boulder,
1286   https://doi.org/10.25811/k3w6-pk81, 2023.
1287 Zinner, T., Schwarz, U., Kölling, T., Ewald, F., Jäkel, E., Mayer, B. and Wendisch, M., 2019: Cloud geometry from
1288   oxygen-A-band observations through an aircraft side window, Atmos. Meas. Tech., 12, 1167-1181,
1289   https://doi.org/10.5194/amt-12-1167-2019.

1290

1291

Appendix

A. Supplementary figures

Appendix A contains supplementary information to complement the details of the simulation setting. These elements cover various topics, from atmospheric profiles and cloud-related parameters to radiative transfer simulations.
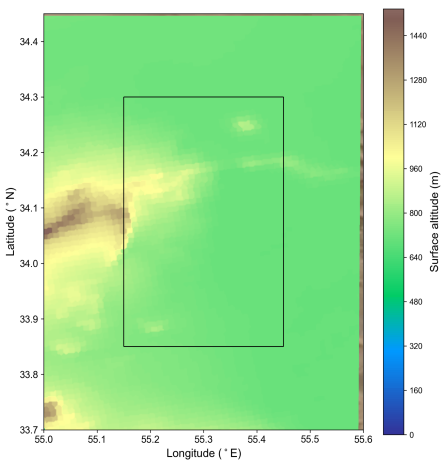
Figure A1: Contour plot showcasing surface height from the MODIS MYD03 file for the outer simulation domain and the inner analysis domain.
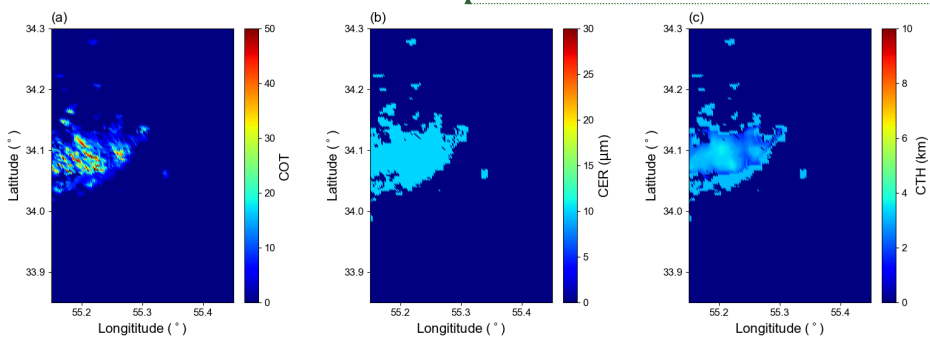
Figure A2: The cloud optical thickness (a), cloud liquid effective radius (b), and cloud top height (c) for the 3D simulation at 650 nm.

Moved down [1]: ¶

Figure A2: (a) Skew-T diagram of the atmosphere and (b) CO_2 and H_2O VMR profiles of Fig. 1 scene.¶
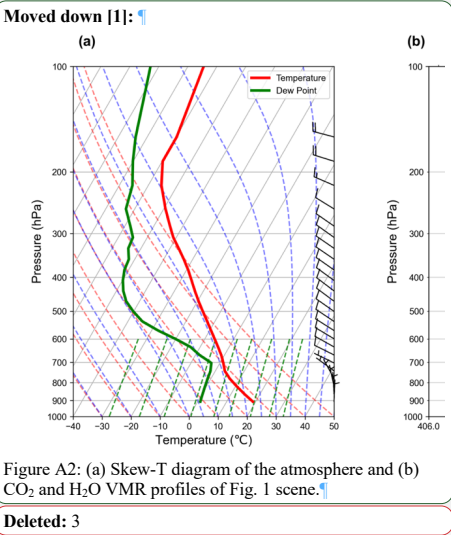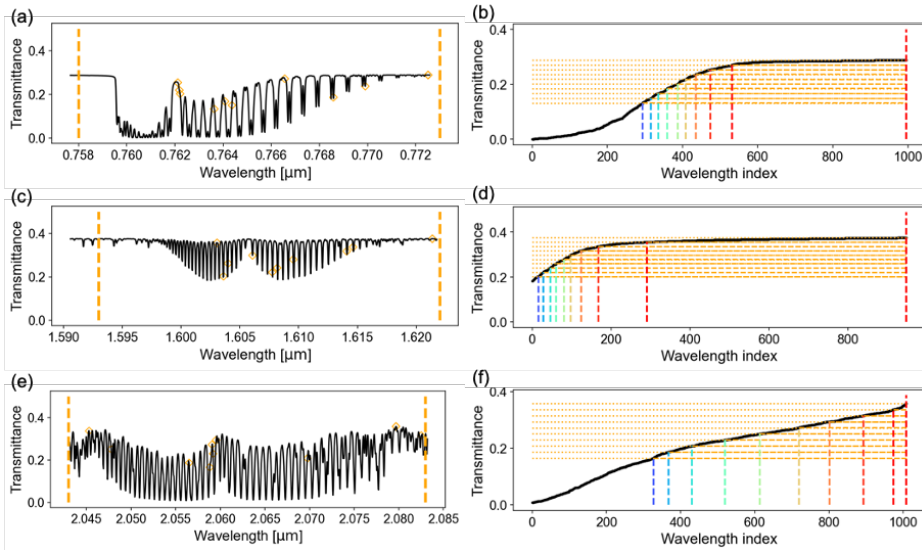
Figure A3: Simulated transmittance of (a) O_2-A, (c) WCO_2, and (e) SCO_2 bands derived from the atmospheric structure presented in Fig. B1. Right panels present the sorted transmittance with the selected wavelength index for (b) O_2-A, (d) WCO_2, and (f) SCO_2 bands. The orange markers on the left panels denote the corresponding selected wavelengths shown in the right panels.
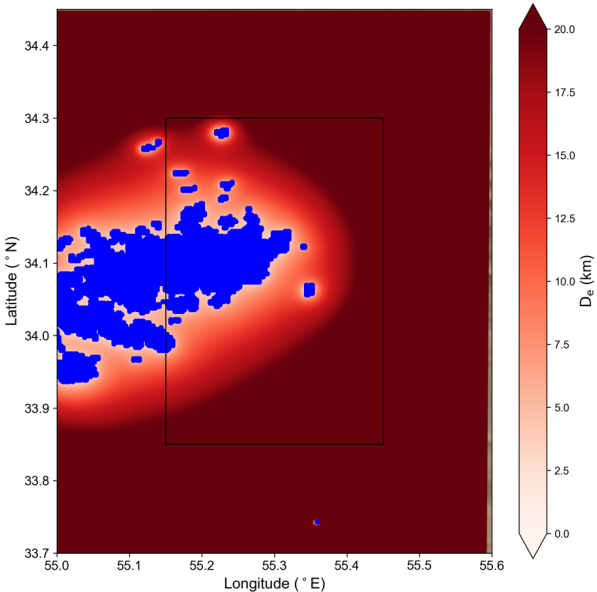
1332
1333 Figure A4: Distribution of the effective cloud distance, with blue dots marking the positions of the clouds. The black
1334 rectangle designates the analysis domain, while the entire domain represents the region of the RT simulation.

1335
1336
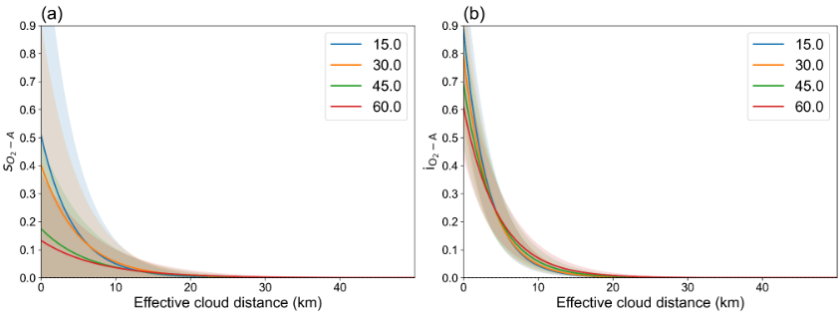
1337
1338 Figure A5: Parameterization of (a) slope and (b) intercept for O_2-A band with effective cloud distance, varied by
1339 solar zenith angle, while holding surface albedo constant.

1340
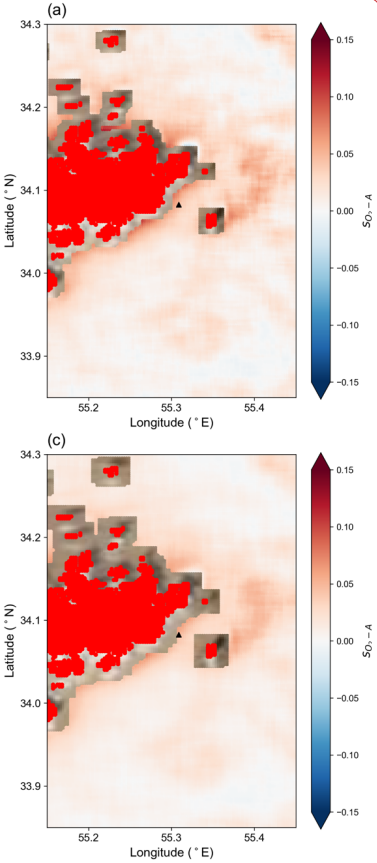
Figure A6. Distribution of s (left) and i (right) for the O_2-A band computed using average radiance from the (a, b) 9×9 and (c, d) 13×13 grid points. Red dots indicate the cloud pixels employed in the RT simulation.
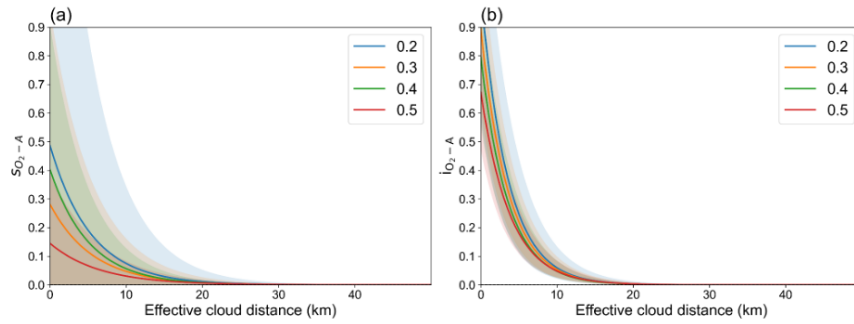
Figure A6: Parameterization of (a) slope and (b) intercept for O_2-A band with effective cloud distance, varied by surface albedo while holding solar zenith angle constant.
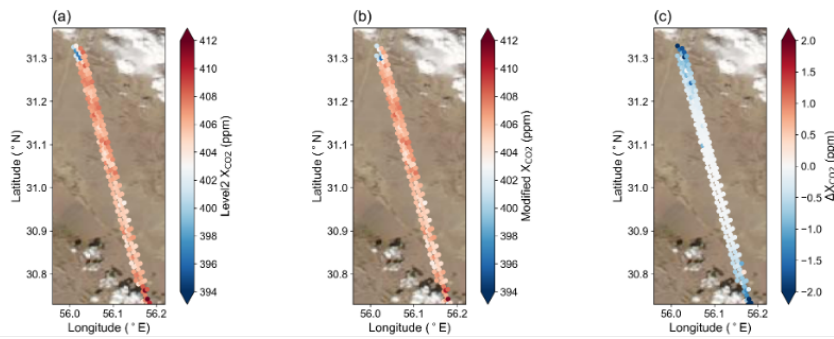
Figure A7: Satellite true-color imagery of MODIS Aqua from NASA Worldview on 5 October 2019 with (a) X_{CO2} in OCO-2 level 2 data, (b) mitigated X_{CO2} retrieved from the adjusted spectra, and (c) difference between the mitigated and original X_{CO2} values.
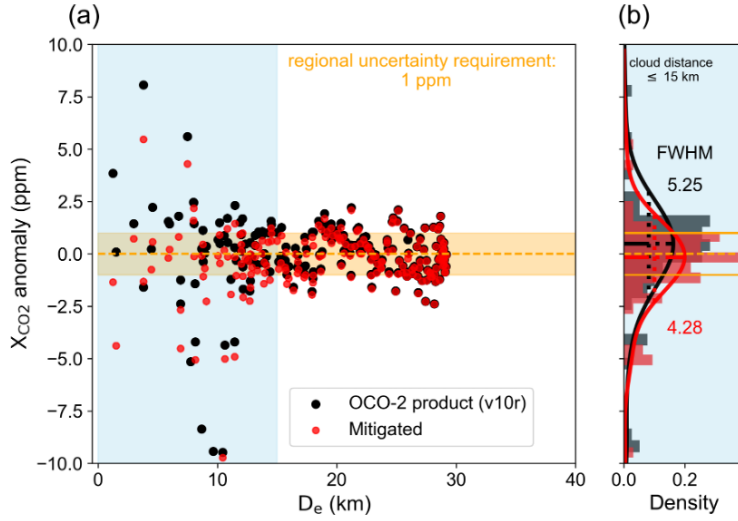
Figure A8: (a) Scatter plot comparing the X_{CO2} anomaly of the OCO-2 L2 product (in black) to its value post-spectra adjustment (in red) for the case shown in the figure above, plotted against D_e. The X_{CO2} anomaly is defined as retrieved X_{CO2} – true X_{CO2}, with the true X_{CO2} defined by the average X_{CO2} of footprints with a D_e greater than 15 km (405.96 ppm in this case). The orange shade indicates the 1 ppm mission requirement. (b) Histograms and probability density functions (PDFs) for the X_{CO2} anomaly of the OCO-2 L2 product (in black) and post spectra adjustment (in red) for D_e within 15 km. This corresponds to the blue-shaded region in (a). The FWHM values of the PDFs of v10r and adjusted data points are 5.25 and 4.28, and the PDF averages are 0.93 and 0.18, respectively. The average change in X_{CO2} after the spectra adjustment for D_e less than 15 km is -0.86 ppm.
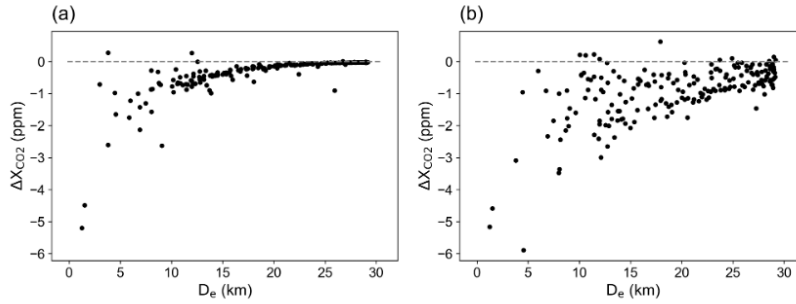
Figure A9: (a) Relationship of ΔX_{CO2} with De based on parameterized slopes and intercepts from the bypass method in Table 2. (b) Corresponding relationship using slopes and intercepts derived from the baseline approach for Fig. A7.

B. Radiative Transfer Simulations

B.1 Vertical atmospheric structure

The atmosphere profile for the simulation is constructed based on the OCO-2 Met and CO_2 prior data, and it is vertically divided into 29 layers. The surface altitude and pressure are determined by the average surface height of the footprints analyzed. The heights of other layers are then linearly interpolated from the surface to 5 km for 11 points, with 0.5 km intervals from 5 km to 10 km, 1 km intervals from 10 km to 14 km, and 5 km intervals from 20 km to 40 km, which was the top height of the simulation. The pressure profile corresponding to these heights is calculated using a method similar to the MERRA-2 reanalysis product (Bosilovich et al., 2015) from NASA's Global Modeling Assimilation Office (GMAO). The temperature and horizontal wind profiles are then retrieved from the OCO-2 Met data by linear interpolation between pressure and temperature/wind.

Accurate number densities of O_2, CO_2, and water vapor are crucial for calculating the absorption coefficients. We assumed that the atmosphere followed the ideal gas law to estimate the number density of each layer. O_2 number density is determined by multiplying its dry-air mixing ratio (0.20935, OCO-2 L2 ATBD) with the dry-air number density. CO_2 number density is calculated similarly by using the CO_2 prior profile. We use the specific humidity in the OCO-2 Met data as well as the temperature and pressure to derive the water vapor volume mixing ratio (VMR) profile. H_2O VMR is essential to obtain more accurate absorption coefficients to consider the water vapor broadening, which is discussed further in Session 3.2.2. The H_2O VMR profile is also converted into number density for further absorption calculation. The derived profiles are displayed in Fig. B1. These steps ensure that the atmospheric parameters used in the simulation are as accurate as possible.
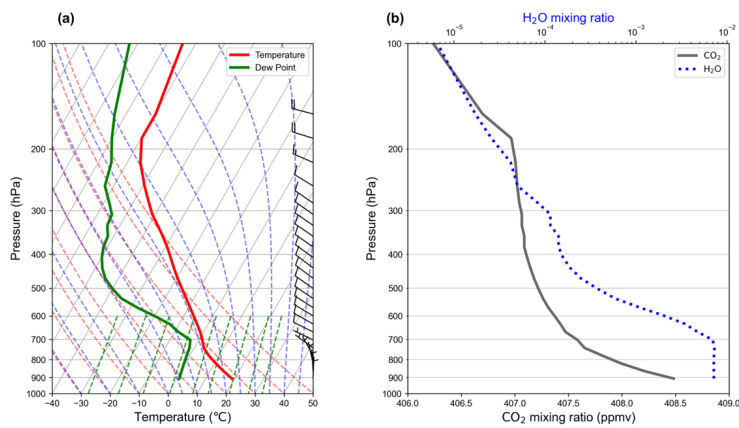
Figure B1: (a) Skew-T diagram of the atmosphere and (b) CO_2 and H_2O VMR profiles of Fig. 1 scene.

B.2 Absorption Coefficients

For missions with high spectral resolution, such as GOSAT and OCO, accurate absorption coefficients within the observed range are indispensable for meticulously modeling the absorption process. This study utilizes the same precalculated lookup tables of absorption coefficients (ABSCO tables) employed in version 10 of the OCO retrieval

algorithm (ABSCO V5.1, Payne et al., 2020). These ABSCO tables furnish line-by-line absorption cross-sections for O_2, CO_2, and H_2O within the observed wavelength range. They also account for line mixing, speed dependence of molecular collisions, and collision-induced absorption (OCO L2 ATBD, 2021). Due to the design of OCO instruments and the varying viewing angles of the eight footprints within the same swath, the wavelengths of each band exhibit slight discrepancies (OCO L1B ATBD, 2021). To mitigate excessive computational demands, we opt to use solely the wavelengths of the first footprint.

The ABSCO tables are functions of the pressure, temperature, and water H_2O VMR. Because the grid points of pressure, temperature, and H_2O VMR are discrete, we calculate the absorption coefficients by applying trilinear interpolation to approximate the cross-section of each line. The instrument line shape provided in the OCO L1B file was used to weigh various lines when calculating the absorption coefficient for each wavelength. With the molecule number densities of O_2, CO_2, and water vapor established during step 3.2.1, we compute the absorption coefficients in km^{-1} for O_2-A, WCO_2, and SCO_2 for lines whose relative cross-section exceeded 0.05 compared to the largest within the instrument lineshape range. The clear-sky transmittance for each wavelength can be calculated using the derived absorption coefficients.

B.3 Cloud detection and properties

MODIS products provide cloud mask information with a cloud identification accuracy of about 90% over land between 60°N and 60°S (Frey et al., 2020). However, undetected clouds can lead to a significant radiance inconsistency in RT simulation for a small footprint. To address this, we detect clouds based on the reflectance difference between the observation and white-sky surface albedo provided by the MODIS 43 product. We use various reflectance thresholds for different cases to ensure that most clouds are detected. This cloud detection approach is distinct from the method used by Chen et al. (2023) and is specifically designed for this study.

Once the cloudy pixels are identified, we retrieve the cloud top height (CTH) of the nearest location from the MODIS MYD02 cloud file and assign it to each cloudy grid point. The cloud effective radius (CER) is manually set to 10 μm for low clouds and 25 μm for high clouds in this study. We plan to use the actual MODIS CER values in future versions to capture more realistic variations. To determine each pixel's cloud optical thickness (COT), we run the RT model over several COTs and derive the COT-radiance relationship by ourselves to ensure the radiance consistency in 1D-RT simulation. The COT of each pixel is then determined by applying the COT-radiance relationship. To adjust for the projection and observation time difference between OCO-2 and MODIS Aqua, we apply a cloud position adjustment as described by Chen et al. (2023). The adjustment includes a geometry parallax shift of the cloud position due to the time shift, wind speed, and direction determined by CTH.

By necessity, this study assumes fixed cloud geometric thickness (1 km for cloud top height smaller than 4 km and cloud base at 3 km for cloud top height greater than 4 km). The additional photon path caused by multiple scattering within clouds influences the magnitude of the 3D cloud effect, so the slopes are sensitive to the choice of geometric cloud thickness. Unfortunately, this parameter is not readily available from operational products. Some attempts are being made to exploit the O_2-A channel of OCO-2 (Zinner et al., 2019; Li et al, 2024). Once these are mature, the information will be used by our algorithm. Generally, since the vertical cloud properties can influence the magnitude and distribution of the 3D cloud effect, further investigation of the impact of cloud properties, including COT, CTH, and cloud base height, on the 3D cloud effect is recommended for future research.

B.4 RT model and tools

This research uses a modified version of the Education and Research 3D Radiative Transfer Toolbox v0.1.1 (Chen et al., 2023) for OCO (EaR^{3}T-OCO) to model the 1D and 3D radiances of the scene. The Monte Carlo Atmospheric Radiative Transfer Simulator version 0.10.4 (MCARaTS, Iwabuchi, 2006) serves as the core engine for this simulator, which automatically ingests satellite products and simulates 1D and 3D spectral radiances. MCARaTS iteratively traces the path of each photon and calculates the distribution of photons based on the final probability. Chen et al. (2023) demonstrate the ability of EaR^{3}T to simulate the radiance observed by OCO-2. We utilize the framework and

example application one outlined in Chen et al. (2023) to develop a specialized version of the application, which is described in Appendix B. We improve the atmospheric structure based on the OCO-2 level 2 products and the absorption coefficient derivation method, as described in Sections 4.2.1 and 4.2.2. For the simulation of each wavelength, 1×10^9 photons are used and distributed to various absorption lines for a single run. The mean radiance and the standard deviation are then calculated from three runs to estimate the uncertainty.

1452 C. Code walkthrough

1453 The codes utilized for this study can be accessed from GitHub at: https://github.com/ywchen-tw/OCO2.
1454 Subsequent sections specify the configuration file settings and provide an overview of the simulation and analysis
1455 process.

1456 C.1 Configuration file

1457 The configuration file in CSV format controls the changeable parameters for the EaR³T-OCO simulation. The
1458 following table describes the meaning and data type of each variable. If a variable is not required to be specified,
1459 the default value is used.
1460

Parameter name	Description	Datatype	Required
descriptor	Case description	string	Y
date	Date of interest	integer, YYYYMMDD	Y
juld	Julian date of the year	integer	
pngwesn	Region for retrieving the MODIS RGB image	4 floats	Y
subdomain	Region for analysis	4 floats	Y
path_sat_data	directory of satellite files	string	Y
l2	File name of geolocated X_{CO2} retrieval results data	string	
lt	File name of OCO-2 Level 2 bias-corrected X_{CO2} and other select fields from the full-physics retrieval aggregated as daily files	string	
l1b	File name of calibrated, geolocated OCO-2 science spectra	string	
dia	File name of geolocated X_{CO2} retrieval results plus algorithm diagnostic information	string	
met	File name of OCO-2 Level 2 meteorological parameters interpolated from global assimilation model for each sounding	string	
imap	File name of geolocated retrieved values of X_{CO2} and fluorescence generated by the IMAP-DOAS algorithm	string	
co2prior	File name of OCO-2 Level 2 CO_2 prior based on CO_2 monthly flask record, global meteorology, and age of air	string	
sol	File name of the solar spectra	string	
nx	Interval of selected wavelength	Integer, default = 5	
Trn_min	Minimum ratio of the largest transmittance for wavelength selection	float, $0 \leq$ Trn_min < 1, default = 0	
abs_interpolation	Option for doing the interpolation	"single", "linear", or	

		"trilinear", default = "trilinear"	
_aerosol	Add a homogeneous aerosol layer	TRUE or FALSE	
asy	Aerosol asymmetry parameter	float	
cth_thick	Cloud top height for thick clouds (km)	float	
cgt_thick	Cloud geometric thickness for thick clouds (km)	float	
cth_thin	Cloud top height for thin clouds (km)	float	
cgt_thin	Cloud geometric thickness for thin clouds (km)	float	
cot_Nphotons	Number of photons used for COT-Ref relationship simulation	float	
path_out	Directory of output files	string	
o2	File name of O_2-A band simulation output	string	
wco2	File name of WCO_2 band simulation output	string	
sco2	File name of SCO_2 band simulation output	string	
retrieval	Retrieval version		
ref_threshold	Radiance threshold @ 470 nm as cloudy pixel	float	Y
modis_650_N_photons	Number of photons used for 650 nm simulation	integer	Y
oco_N_photons	Number of photons used for OCO 3 bands simulation	integer	Y

1469
1470

1474 C.2 Preprocess
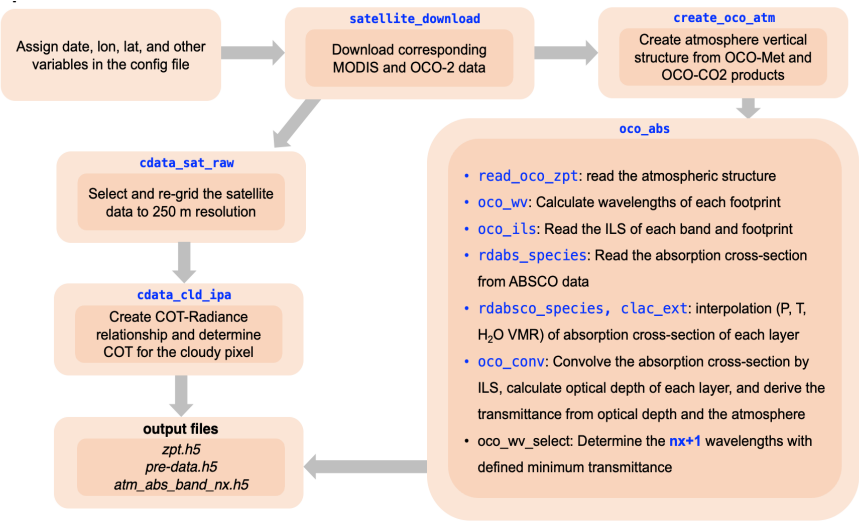
1475
1476
1477 The oco_simulation.py code is the main code for data acquisition and radiance simulation. Here, we focus on the first
1478 part of the code (the preprocess function), which deals with data download and preprocessing.
1479

1480 1. satellite_download function: This function accesses the configuration file variables, subsequently
1481 downloading the pertinent MODIS and OCO-2 data as dictated by the specified date and geolocation details.
1482 2. create_oco_atm function: Leveraging OCO-2 data, this function constructs vertical profiles for temperature,
1483 water vapor, and wind.
1484 3. oco_abs function: Based on the atmospheric profiles, this function computes the optimal absorption coefficients
1485 for all three OCO-2 bands, subsequently identifying the wavelengths for simulation.
1486 4. cdata_sat_raw function: Extracts data from the MODIS and OCO-2 files, then restructures this data to a 250
1487 m resolution.
1488 5. cdata_cld_ipa function: Using the EaR³T simulator, this function establishes a COT-radiance relationship and
1489 designates a COT for every grid point.
1490
1491 Upon completion of the preprocessing stage, the system will generate the following files:
1492
1493 ● *zpt.h5*: Details the vertical atmospheric structure.
1494 ● *pre-data.h5*: Contains information on cloud and radiance.
1495 ● *atm_abs_band_nx.h5*: Captures data on the absorption coefficients.
1496
1497
1498 C.3 Simulation
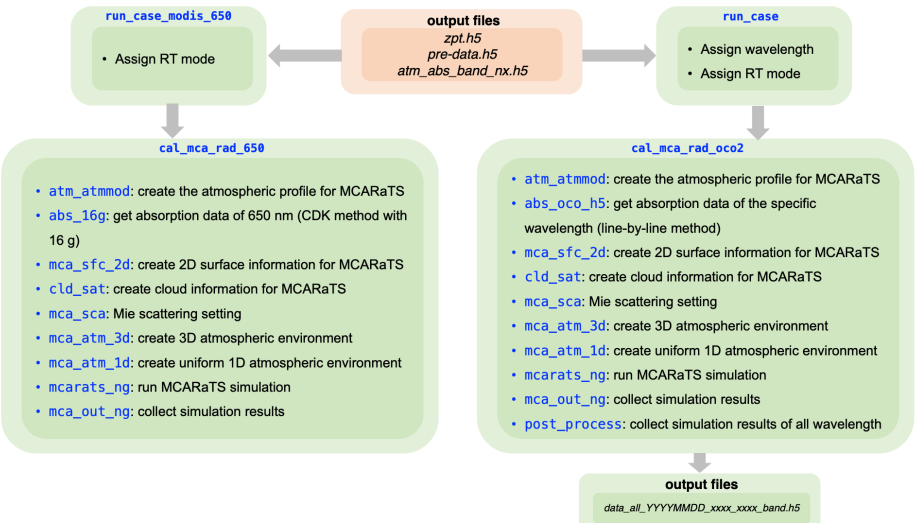
1501
1502
1503 The second part of the oco_simulation.py code (run_case_modis and run_case functions) is primarily concerned with
1504 radiance simulation.
1505
1506 1. run_case_modis function: This function drives the EaR^{3}T simulator to simulate radiance at 650 nm, operating
1507   in either the IPA or 3D modes. It employs the correlated-k distribution method, as detailed in Chen et al. (2023).
1508   Upon completion, simulation results are stored in the ***post_data.h5*** file.
1509 2. run_case_oco function: This function activates the EaR^{3}T simulator to simulate radiance for each designated
1510   wavelength, as identified by the oco_abs function. It utilizes the IPA mode for clear-sky simulations and the
1511   3D mode for real-world conditions. The respective simulation outcomes for each band are archived as
1512   ***data_all_YYYYMMDD_xxxx_xxxx_band.h5***.
1513
1514 C.4 Postprocess

Formatted: Superscript

Deleted: mode

Deleted: the
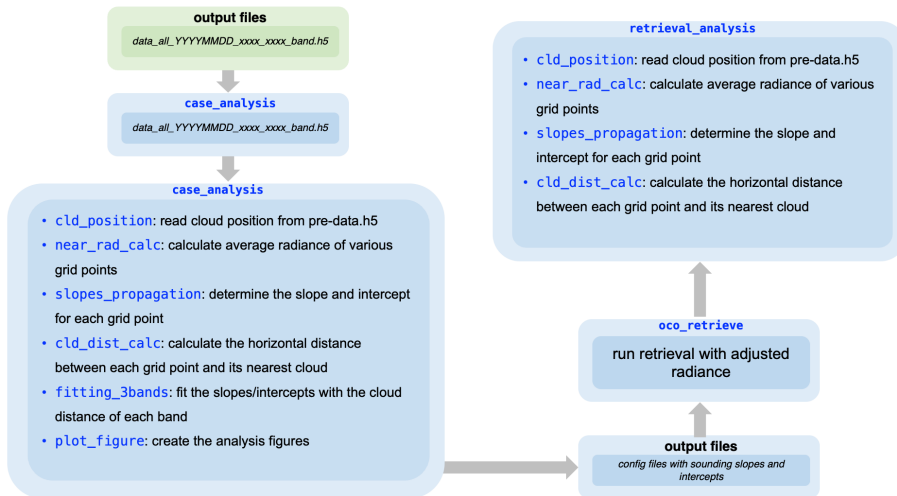
Following the radiance simulation, we proceeded with an analysis leveraging the case_analysis.py code, and subsequently executed oco_retrieve.py to extract the mitigated X_{CO2}.

1. case_analysis function: This function accesses the output files from the radiance simulation and computes the mean radiance across various average sizes, a process managed by the near_rad_calc function. Next, the slopes_propogation function determines the slope and intercept for each grid point. With the help of the weighted_cld_dist_calc function, the effective cloud distance for each grid point is gauged based on cloud positioning. The fitting_3bands function determines the most suitable fitting coefficients for the 3D parameters and the effective cloud distance. Following this, the effective cloud distance for every footprint is established and used to derive the corresponding parameterized slopes and intercepts. All results are consolidated in the configuration file.
2. oco_retrieve function: Initially, this function adjusts the radiance of the footprint in line with the set slopes and intercepts. It then triggers the OCO retrieval algorithm with the modified spectra to obtain the mitigated X_{CO2}.
3. case_retrieval_analysis function: This function reviews the output of the mitigated XCO2 and juxtaposes the findings with the OCO-2 L2 product.